Real-time Regularized Tracking of Shear-Wave in Ultrasound Elastography

Mahmoud Derakhshan Horeh

A Thesis

in

The Department

of

Electrical and Computer Engineering

Presented in Partial Fulfillment of the Requirements

for the Degree of

Master of Applied Science (Electrical Engineering) at

Concordia University

Montréal, Québec, Canada

September 2017

CONCORDIA UNIVERSITY

School of Graduate Studies

This is to certify that the thesis prepared

By: **Mahmoud Derakhshan Horeh**

Entitled: **Real-time Regularized Tracking of Shear-Wave in Ultrasound Elastography**

and submitted in partial fulfillment of the requirements for the degree of

Master of Applied Science (Electrical Engineering)

complies with the regulations of this University and meets the accepted standards with respect to originality and quality.

Signed by the Final Examining Committee:

_____ Chair
Dr. Rabin Raut

_____ External Examiner
Dr. Tiberiu Popa

_____ Examiner
Dr. Otmane Ait Mohamad

_____ Supervisor
Dr. Amir Asif and Dr. Hassan Rivaz

Approved by _____
William E. Lynch, Chair
Department of Electrical and Computer Engineering

_____ 2017

_____
Amir Asif, Dean
Faculty of Engineering and Computer Science

Abstract

Real-time Regularized Tracking of Shear-Wave in Ultrasound Elastography

Mahmoud Derakhshan Horeh

Elastography is a convenient and affordable method for imaging mechanical properties of tissue, which are often correlated with pathologies. An emerging novel elastography technique applies an external acoustic radiation force (ARF) to generate shear-wave in the tissue which are then tracked using ultrasound imaging. Accurate tracking of the small tissue motion (referred to as tissue displacement) is a critical step in shear-wave elastography, but is challenging due to various sources of noise in the ultrasound data. I formulate tissue displacement estimation as an optimization problem and propose two computationally efficient approaches to estimate the displacement field. The first algorithm is referred to as dynamic programming analytic minimization (DPAM), which utilizes first order Taylor series expansion of the highly nonlinear cost function to allow for its efficient optimization. DPAM was previously proposed for quasi-static elastography and I extend the approach to shear-wave elastography. The second algorithm is a novel technique that exploits second-order Taylor expansion of the non-linear cost function. I call the new algorithm as second-order analytic minimization elastography (SESAME). I compare DMAP and SESAME to the standard normalized cross correlation (NCC) approach in the context of estimating displacement and elasticity of the medium for shear-wave elastography (SWE). The results of micrometer-order displacement estimation in a uniform simulation phantom illustrate that SESAME outperforms DPAM, which in turn outperforms NCC in terms of signal to noise ratio (SNR) and jitter. In addition, the relative difference between true and reconstructed shear modulus (averaged over several excitations focussing at different focal depths with different scatterers realizations at each depth) is approximately 3.41%, 1.12% and 1.01%, respectively, for NCC, DPAM and SESAME. The performance of the proposed

methods is also assessed with real data acquired using a tissue-mimicking phantom, wherein, in comparison to NCC, DPAM and SESAME improve the SNR of displacement by 7.6 dB and 9.5 dB, respectively. Experimental results on a tissue-mimicking phantom also show that shear modulus reconstruction is more accurate with DPAM and SESAME in comparison with NCC.

Acknowledgments

Dr. Amir Asif: I will never forget the first day I met you in your office. I had arrived to Montreal just the day before. I came to your office and secretary asked me to have a sit and wait to meet you. I was checking messages in my cellphone that you touched my shoulder and asked Mahmoud? I was too stressful for the first time. You came all the way from your office to waiting sits in the entrance of Dean's office to pick me up. I will never forget it. Meetings came back to back every week but you were always treated me too respectfully. Beside technical aspect of research that I learned a lot from you; you always will be a symbol and example of a real gentleman in my mind forever. Thank you for giving me your knowledge and time. That is my pleasure.

Dr. Hassan Rivaz: Studying and working under your supervision is an unforgettable experience for me. You always behaved me the way I always wish for every student to be behaved by his/her supervisor. More than being supervisor, I always felt you as a real friend for myself. You Accompanied me in every step of this way. Even when the research was not progressive enough, you always encouraged me to fight and fight and fight. The way you motivate your students is highly exemplary. I want to thank you again for everything. Merci Hassan!

Dad: Dad you've taught me how to respond to challenges I face in my life. Always try to do your best. you always have told me a successful person is not whom he/she has achieved a lot in life, but a successful person is one who is satisfied by the effort he/she puts in life. Now I again remind myself your advice. I'm satisfied so I'm successful Dad. Thank you for every single second you were with me. You will be the biggest hero in my life.

Mom: Maman! You give me everything you have. I left you and came to Montreal to do my Masters but my heart always beats for you. I always miss you mom. I never forget how happy I was

when I wanted to see you on video chat. I do not want to be far from you and for myself, I ask God to let me see you soon and never be without your love and support. $Asheghetam\ Maman$.

Colleagues: I would like to highly appreciate all of my colleagues in image processing lab at Concordia university. Without their help and supports, this work was not possible. I will never forget our memories and for all of you, I wish the best in your life. Special thanks to Parviz Khavari who helped in collecting data in PERFORM Centre, Concordi university, Montreal, Canada.

Others: The authors would like to thank Julian Lee from Alpinion Ultrasound for technical support and for loaning the L3-8 transducer as well as Mark Palmeri for providing the shear-wave simulation data. The work presented in this paper is supported by NSERC Discovery Grants RGPIN-2017-06629 and RGPIN-2015-04136.

Contents

List of Figures

List of Tables

Chapter 1

Thesis Overview

1.1 Motivation

In 2015, the Cancer Research Society (CRS) organization, based on statistics achieved from previous years, predicted the number of citizens who would suffer from cancer in Canada in their lifetime as well as the expected number of people who will face cancer and the total number of deaths caused by cancer in 2016. The following list of information is what comes out from their research and statistics:

- One in two Canadians will face cancer or develop it in their lifetime.
- 202,400 expected cases of cancer will be found in 2016.
- Every 3 minutes, a new case of cancer will be diagnosed.
- Since 2005, cancer is the main reason of death in Canada.
- One in four Canadians dies because of cancer.
- 78,800 expected cases of deaths caused by cancer in 2016 alone.
- 9 people per hour die for a reason related to cancer development in Canada in 2016 alone.
- The most frequent types of cancer in men are prostate, colorectal and lung.
- The most frequent type of cancer in women are breast, lung and colorectal.

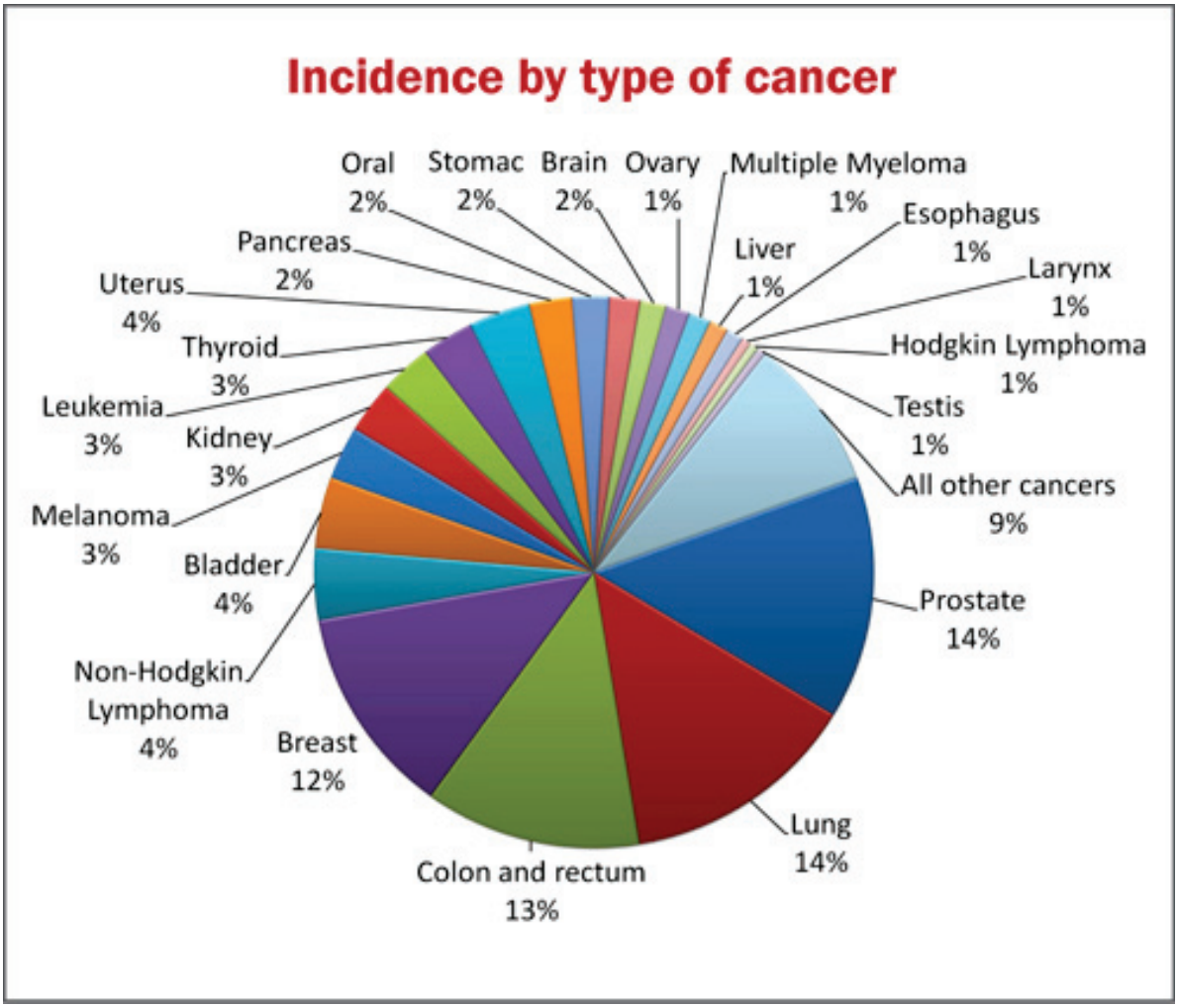

Figure 1.1: Statistics regarding distribution of cancer types in Canada in 2016. As shown above, more than half of the cases are prostate, lung, colorectal and breast cancers. This image is taken from CRS organization website CRS-SRC (2017).

Fig. 1.1 categorizes different types of cancer in Canada in 2016. As shown in the figure, more than half the cancers are prostate, lung, colon and rectum (colorectal), and breast cancers. An important point that should be noted is the fact that all these four parts of the body are composed of soft tissue. In other words, soft tissue in the body is the most immune to growth of cancerous cells. In addition, prostate cancer as the most common case of cancer in men, and breast cancer in women, both are considered to be the most soft tissue in the body. Therefore, research on understanding cancer in soft tissue, clinical diagnosis, and treatment will help greatly to control cancer in people in the coming years.

During the past years, many methods have been developed and even commercialized based on different image modalities, such as MRI, CT and Ultrasound. Both MRI and CT are commonly used in cancer diagnosis and many successes have been yielded using these devices. Ultrasound has been recently introduced for cancer diagnosis. Portability, low price, ease of use, and real-time capability are the most significant reasons for using ultrasound for the diagnosis of cancer.

The idea of utilizing ultrasound for diagnosis of stiffer parts vulnerable to be as tumor started approximately 20 years ago. The initial work of Ophir et al. (2000) and Sarvazyan et al. (1998) explored this possibility. To investigate mechanical properties of tissue, the tissue should be deformed and deformation should be tracked using an ultrasound scanner. Since harder regions (tumor) in tissue are less compressible as compared to soft tissue (healthy parts), the strain of the tissue could be estimated. Strain is the relative map of stiffness under imaging. This technique is called elastography, which results in an elasticity map of the tissue at the end of the process. Although elastography techniques have improved in the past years, there are still several challenges. Nowadays, even on the most recent commercial ultrasound machines which have the ability of performing elastography in real-time, many inaccurate elasticity estimations are observed. This means in real cases where a real patient who suffers from cancer is imaged, ultrasound scanner is not able to provide an accurate map of elasticity to determine the location of the tumor. Inaccurate estimation often result due to the limitations in correlation-based methods used to track tissue deformation.

In this thesis, two novel approaches in tracking deformation are proposed which significantly increase the accuracy of tracking tissue deformation. In fact, the focus of this thesis is on displacement

estimation as the most important step in elastography. In some techniques of elastography, deformation of tissue measured in order of micrometer, which is beyond the capacity of the state-of-art correlation-based methods. In addition, noise added from different sources make the estimation even more difficult. My proposed algorithms for tracking deformation are based on introducing an error function and minimizing this function in order to find displacement. Heart of the implementation is done in C++ while MATLAB is used for processing and displaying the results.

1.2 Thesis Structure

The following bulleted list provides an overview and summary of chapters included in this thesis:

- Chapter 2 explains basic concepts of ultrasound imaging. It starts with a discussion of the physics of ultrasound probe and then explains the methodology used for image construction in ultrasound. Afterward, a few applications of ultrasound are presented. As a very important application, elastography has been used and applied in medical imaging. The two common categories of ultrasound elastography based on how tissue are excited are then explained.

- Chapter 3 reviews relevant concepts of Acoustic Radiation Force (ARF) based imaging as a dynamic type of elastogrphy. Acoustic Radiation Force Impulse (ARFI) imaging and Shear-Wave Elastography (SWE) as the most important techniques of Acoustic Radiation Force (ARF) based imaging are then presented. A review of common methods used for displacement and elasticity estimation are presented. After mentioning the drawbacks of these methods, my proposed approaches are presented.

- Chapter 4 first explains a correlation-based method for displacement estimation and then introduces a regularization-based approach. Dynamic Programming (DP) and Dynamic Programming Analytic Minimizations (DPAM) are explained as methods to estimate integer and subsample displacements, respectively. Afterward, Second-order Analytic Minimization Elastography (SESAME) which incorporates more information compared to DPAM is introduced to further improve the accuracy of displacement estimation. The validation and

computational complexity of the proposed methods are discussed close to the end of the chapter.

- Chapter 5 presents results from both simulation and real data to assess the accuracy and precision of the proposed methods. Simulation data is created using Field II software for excitation at different depths and with different materials. Results of both displacement and elasticity are presented. In addition, real data is used in two scenarios: first, in a uniform medium and second, in a medium containing a lesion to assess the accuracy of the proposed methods and also to compare them with Normalized Cross Correlation (NCC), a commonly used correlation-based method.

- Chapter 6 discusses the results obtained and makes overall obseravtion on the advantages and limitations of the proposed approaches.

- Chapter 7 summarizes the thesis and presents a few directions for future work.

Chapter 2

Introduction

In order to utilize ultrasound technology for diagnosis in medical field, a basic understaing of how ultrasound works and collects data from a tissue under imaging is essential. Therefore, in Section 2.1, I first provide some basic information regarding ultrasound probe. Afterward, I introduce ultrasound image construction and a few relevant applications of ultrasound. As a well-known application, ultrasound elastography is presented in Section 2.2. After introducing the basic concepts of elastography, two major types of elastography (static and dynamic) are introduced in the following discussion. At the end, I summarize the chapter in Section 2.3.

2.1 Physics of Ultrasound

Unlike many imaging modalities, ultrasound is highly user-dependent. Therefore, understanding of the principals of ultrasound technology is important for clinicians who work with an ultrasound scanner. Although ultrasound is commonly known as a simple technology, a comparison of ultrasound with radiographic imaging makes the complexity of ultrasound clear. Many pathologists know radiographic imaging very well. In radiographic imaging, x-rays travel directly from a tube at one end towards a detector at the other side. The x-ray intensity on the receiver side determines the specifications of the tissue through which x-rays have propagated.

In ultrasound, the story is somewhat different. In fact, the physical properties of ultrasonic beam determine the relevant details in ultrasound images. Reflection, attenuation and refraction are the

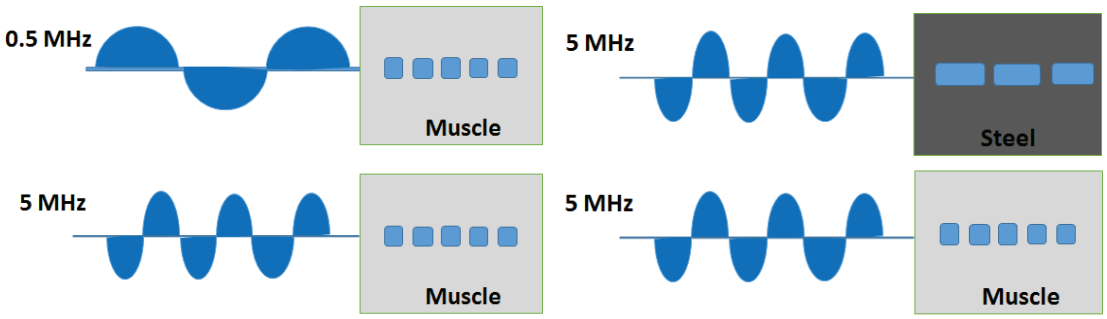

(a) (b)

Figure 2.1: In plot (a), acoustic waves with different frequencies travel at the same speed in the same medium. On the other hand, in plot (b), similar acoustic waves travel with different speeds in different materials.

most significant of them, and they can lead to large artifacts, Aldrich (2007); Redford (2006).

To clearly illustrate the ultrasound behavior, an understanding of some of the significant factors in ultrasound technology is useful. These factors are listed below.

(1) Frequency: number of pressures in 1 sec determines the frequency of ultrasound scanner. This frequency is not relevant to the tissue or any medium which is under imaging, but the ultrasound scanner determines the frequency. Typically, the ultrasound frequency is set to be in the range of 1 to 20 MHz, which is much higher than the range human hearing, Hedrick et al. (1995).

(2) Propagation speed: unlike frequency, the propagation speed for ultrasound is determined by the medium through where the wave travels. The stiffness and density of the medium are two quantities, which determine the propagation speed as depicted in Fig. 2.1. In soft tissue, the propagation speed is typically considered to be 1540 m/sec.

(3) Pulsed ultrasound: determines how the sound waves are transmitted from the source through the tissue. In typical commercial ultrasound scanners, the duration of pulses are in the order of milliseconds and several thousand of the pulses are transmit into the tissue in a single probe.

(4) Interaction of ultrasound with tissue: once a beam propagates through the tissue, different actions happen to the beam. The beam can be reflected with the reflection referred to as the echo in this technique. The reflection is highly relevant in ultrasound diagnosis, Abu-Zidan et al. (2011). As illustrated in Fig. 2.2, reflection happens when the beam arrives

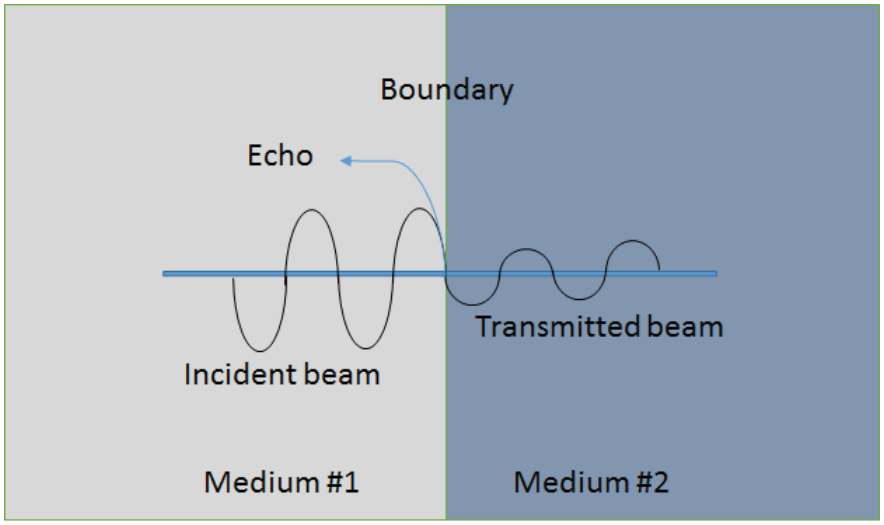

Figure 2.2: Two materials with two different acoustic impedances. Defference of impedances determines the echo amplitude reflected from the boundary. If two boundaries have the same acoustic impedance, no echo will be received.

at the boundary of two materials having different impedances and is calculated using the propagation speed and density. Depending on the difference between the two materials, the echo amplitude varies. The following list indicates how the echo amplitude varies due to impedance difference:

(a) No difference: there will be no echo.

(b) Small difference: a weak echo is received and most of the beam enters the second material.

(c) Large difference: a strong echo is received with only a fraction of the beam entering the second material.

Table 2.1 lists the echo percentage at the boundary of two different types of tissue. As mentioned in the table, in soft tissue where ultrasound is highly suitable, echo produced is very small.

(5) Attenuation: as a matter of fact, refraction, scattering, reflection, and absorption are the most significant factors to cause attenuation of the transmitted beam. Depending on the size of object as compared to the wavelength, one of these actions is more significant. For instance,

Table 2.1: Reflection percentage at boundaries.

Boundary	% Reflected
Fat/Muscle	1.08
Fat/Kidney	0.6
Soft tissue/Water	0.2
Bone/Fat	49
Soft tissue/Air	99

if the object size is very large as compared to the wavelength, refraction and reflection are considerably greater. On the other hand, if this difference is small, then energy of the wave is scattered in many directions. A very important point to mention is that attenuation is directly related to the frequency of ultrasound. This means that a lower frequency should be used if a higher penetration is needed. Since higher resolution is yielded by applying a higher frequency, there is always a trade-off between higher resolution and penetration. For example, a 3 MHz beam after passing 1 cm of the tissue, attenuates 3 dB and for every following centimeter of the tissue attenuates 3 dB. This means that the amplitude of the emitted beam decreases over a million times after passing only 20 cm of the tissue.

Ultrasound probe is the most important part of any ultrasound machine. In the following section, I explain ultrasound probe specifications and functionality in more details.

2.1.1 Ultrasound Probe

Transducer is an equipment in ultrasound used for sending and receiving signal. This device is created using piezoelectric materials and converts electrical energy to mechanical. In one hand, by applying electrical energy to the piezoelectric, a physical perturbation happens in the tissue. On the other hand, a transducer is able to electrically reconstruct the shape when the medium under examination deforms.

Depending on the application, various probes are commercially available. In some of them, probe elements are placed in a line, whereas circular placement is also popular in other applications. In linear arrays, voltage is applied to elements one by one to create a scanning motion pattern. Commercial probes usually consist of 256 elements. Depending on the frequency required, the

width between the elements can be in the range of 1 mm to 10 mm.

An ultrasound probe is normally formed from a disk-shaped crystal which is in the order of a millimeter in diameter and a thickness of 1.8 mm to 0.18 mm for the frequency range of 1 MHz to 10 MHz. As a matter of fact, the frequency depends on the thickness. Basically, as the thickness increases, the frequency decreases and as the thickness decreases, a higher frequency is yielded.

A very important option available in advanced probes is termed as phased array. In phased arrays, all elements of an array emit a pulse simultaneously unlike the linear array in which several of them are fired. The idea in phased array is using delay between transmitted pulses as depicted in Fig. 2.3. This arrangement sets the beam to the desired angle.

2.1.2 Ultrasound Image Construction

Despite many changes applied to ultrasound technology during the past years as a result of enhancement in computer technology, concepts of image production are still similar to the basic models. Echo strength, echo direction, and arrival time of the echo are the most significant factors which a pulse echo system needs to detect. There are several materials having different densities in different depths. Therefore, there might be different echo signals from different boundaries which arrive at separated time steps at the detector. To overcome this issue, differential amplification is considered and applied to weak reflection received from deeper boundaries.

If the object is moving, the frequency of received echo will be affected. In the analysis of Doppler effect, as an object is moving away, the frequency content of the received signal shifts to a lower value. Similarly, if the object moves towards the probe, the frequency increases. This changes in the frequency is typically in the order of a hundred hertz and provides important information mostly on the blood flow.

Normal real-time ultrasound machines should display 15 to 60 frames per second. Given such high frame-rate, every motion which occurs in the tissue will be clearly visible. Increasing the frame rate however, makes the appearance of the motions smoother. Fig. 2.4 shows the real-time ultrasound machine, which is used for data collection in this thesis.

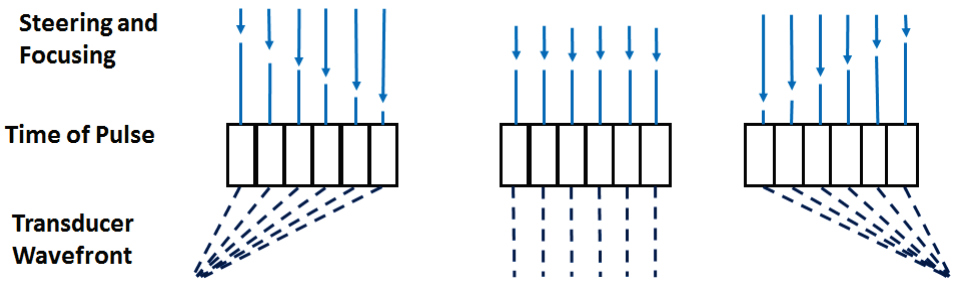

Figure 2.3: Steering and focusing of ultrasound.

Figure 2.4: Real-time ultrasound machine. This image is from Alpinion Medical Systems.

2.1.3 Ultrasound Technology Applications

Since the emergence of the ultrasound technology, many applications have been proposed based on this technology. Being easy to use, affordable, accessible, and real-time operational, ultrasound has attracted researchers and people in industry as well. The more popular applications include:

- Detecting submarines
- Polaroid SX-70 camera
- Automatic door opener
- Industrial non-destructive testing, and
- Quality control
- Medical uses which this thesis focus on this application

Although, ultrasound images are noisy, they have been used in many applications. A very well-known technique in estimating soft tissue stiffness using ultrasound is called ultrasound elastography which is the focus of this thesis.

2.2 Ultrasound Elastography

Elastography, as a medical imaging modality, estimates the tissue elasticity which is highly desired in numerous medical applications such as detecting cancerous tumors in liver, breast, thyroid, prostate, and other soft tissue. In musculoskeletal imaging to estimate the mechanical properties of muscles and tendons, certain elastography techniques have been developed. Generally, every elastography technique includes three major steps as shown in Fig. 2.5. The Radio Frequency (RF) frames are referred to as raw data acquired from ultrasound machine before and after tissue deformation. Next step which somewhat is the most challenging part of elastography, is calculating displacement caused by deformation. At the end, the displacements are transformed into the strain.

During the past two decades, several ultrasound (US) imaging techniques have been proposed to estimate the mechanical properties of the tissue, Catheline et al. (1999); Ophir et al. (2000); Sandrin

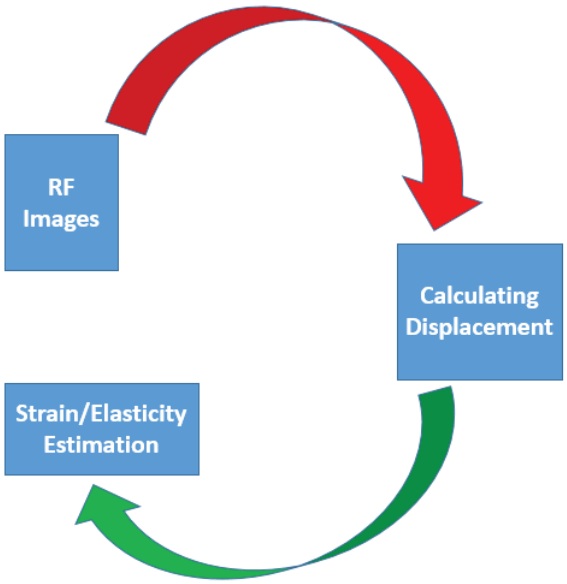

Figure 2.5: Three major steps in elastography.

et al. (2002). These techniques are generally referred to as ultrasound elastography and are broadly categorized into two different groups of quasi-static and dynamic elastography.

2.2.1 Quasi-Static Elastography

In quasi-static elastography (Ophir et al. (2000), pel), a slow, relatively static compression is applied to the tissue. Ultrasound RF signals acquired before and after the compression are correlated to estimate tissue displacements. Fig. 2.6 depicts the compression of the tissue by means of a probe. In order to track the displacement of the scan window (green window), a low uniform compression is applied and tissue is imaged before and after the compression. After collecting images before and after the perturbation, as shown in Fig. 2.7, I calculate the displacements of the pixel values. Depending on the amount of the force applied by compression, displacement can be different. In quasi-static elastography, although lateral (perpendicular to the compression axis) displacement image is important, axial displacement (parallel to the compression axis) has more relative information and is considered as the major displacement happening in the tissue. Therefore, in this case, only the axial displacement profile is studied. Finally, to find the strain image which displays the relative hardness of tissue, I take the derivative of displacement image in the axial

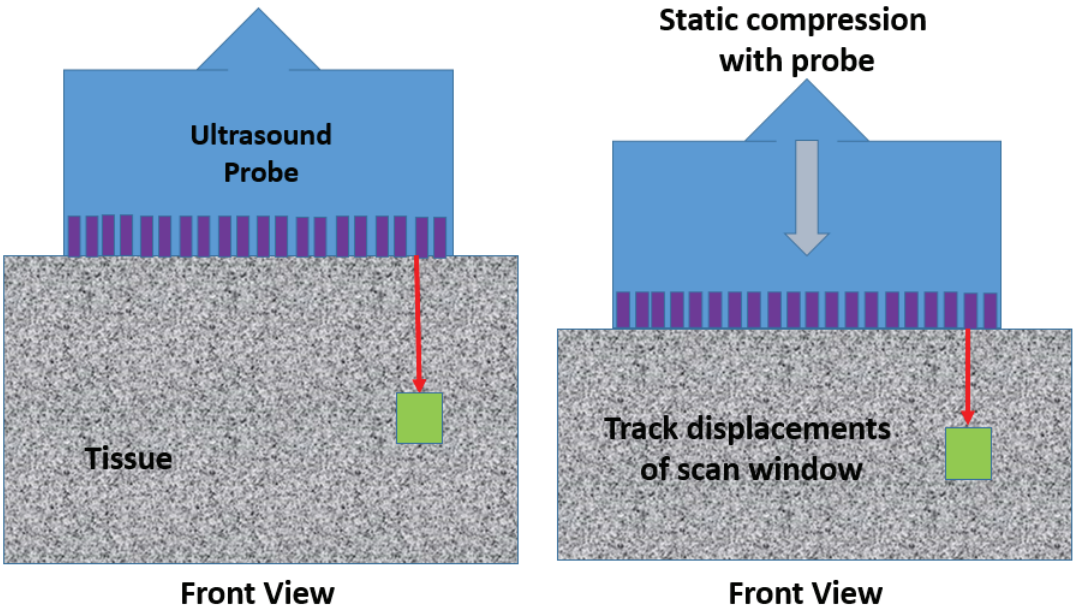

Figure 2.6: Compression and imaging the tissue in quasi-static elastography. An image before compression and an image after compression are acquired. Comparing two frames will enable us for calculate displacement and then strain of the tissue.

direction to obtain the strain image, which shows the exact location of the tumor.

Quasi-static elastography results in a quantitative map of hardness of the tissue. It is however, limited due to manual palpation which causes additional noise to be added to the ultrasound data. In addition, this method is limited to the soft organs where manual palpation is possible.

2.2.2 Dynamic Elastography

In dynamic elastography (Bamber et al. (2013); Bercoff et al. (2002); Catheline et al. (1999); Nightingale et al. (2003); Sandrin et al. (2002); Sarvazyan et al. (1998)), tissue deformation occurs at a faster rate and the propagation of mechanical waves is used to derive the mechanical properties of the tissue. Although both static and dynamic approaches use ultrasound to track the displacements, the difference lies in the applied perturbation, which can be either quasi-static or time-varying.

Fig. 2.8 shows how shear-waves are propagated in the tissue after an Acoustic Radiation Force (ARF) excitation is applied to the tissue. In fact, in dynamic elsatography, the source of deformation is different from quasi-static elastography. Similar to quasi-static, imaging should be done before

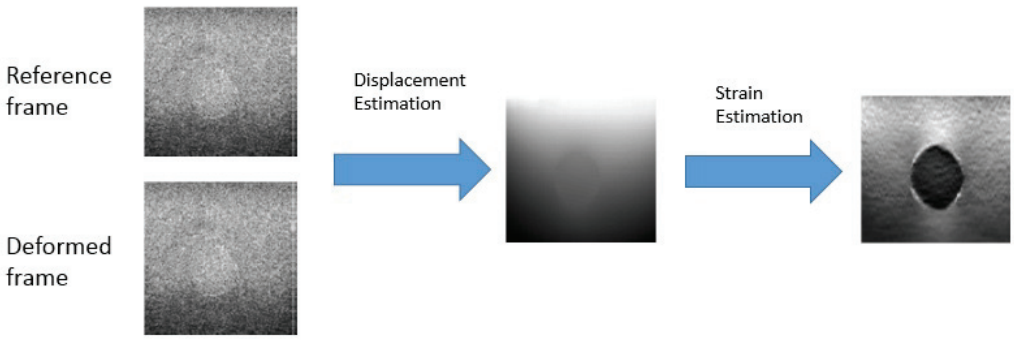

Figure 2.7: An illustration of Quasi-static elastography.

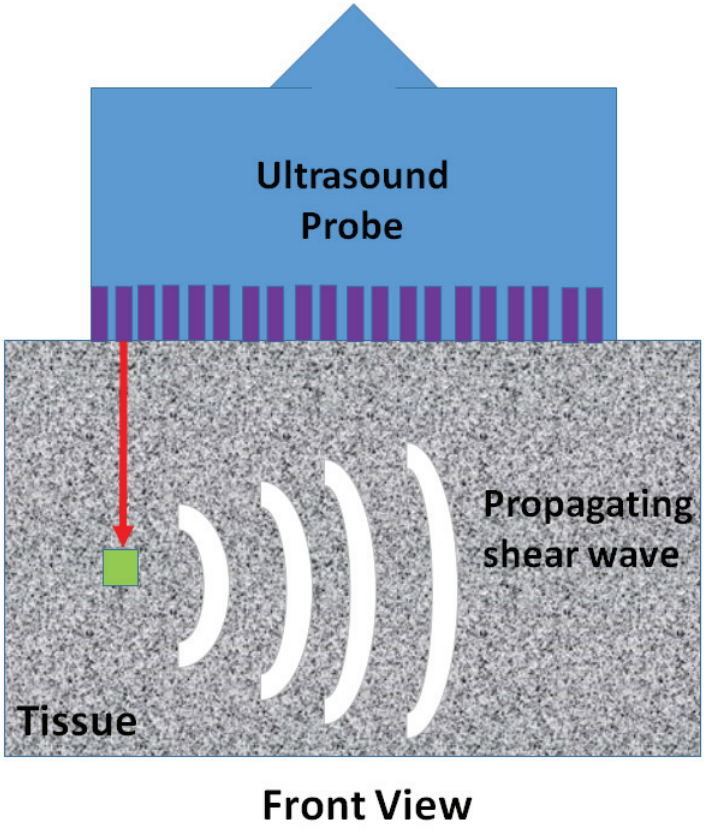

Figure 2.8: Shear wave propagation in the tissue. The probe focuses and excites a point as specified by a green square. Shear wave as a result are propagated in the tissue and the goal to to track the wave motion in shear-wave elastography.

and after tissue deformation. Herein, tissue does not move uniformly. Instead of uniform movement, shear-wave propagates in the tissue. This force, unlike quasi-static, is time varying. Depending on the type of excitation, dynamic elastography itself can be further categorized into several subgroups, including vibro-acoustography, Acoustic Radiation Force Impulsion (ARFI), transient elastography, Shear-Wave Elastography (SWE), etc Gennisson et al. (2013). In the next chapter, I will discuss ARF-based imaging in more details highlighting relative work completed in this field.

2.3 Summary

This chapter started with an introduction to ultrasound physics. The reason is that every person who tends to use ultrasound, whether in the medical field or not, should know basic concepts of this technology. I talked about the ultrasound probe as the heart of ultrasound machine and I mentioned how piezoelectrics in ultrasound probe are placed to determine the frequency. Afterward, I explained how the received echo is used to create an ultrasound image. I also listed a few applications of ultrasound. In next section, I talked about elastography as a new application of ultrasound technology in the medical imaging field. Every elastography technique includes three major steps:

- Imaging the tissue before and after deformation.
- Calculating displacement between pre and post compression image.
- Estimating quantitative or relative strain map of the tissue which indicates where exactly the probable tumor is placed and how stiff it is.

Depending on the type of excitation, elastography techniques are categorized in two groups: 1) Quasi-Static Elastography which applies a uniform force to the tissue and images the tissue before and after the compression; 2) Dynamic elastography, in which, unlike quasi-static, the applied force is time-varying and not uniform. It usually creates shear-wave in the tissue. Tracking the waves results in an estimating of the shear-wave speed, which can be used to estimate strain in the tissue.

Chapter 3

Literature Review of Acoustic Radiation Force-based Elastography

As mentioned in Subsection 2.2.2, depending on the type of excitation, dynamic elastography itself can be further categorized into several subgroups, including radiation-force-based imaging which by itself includes ARFI and SWE that are two well-known techniques in elastography. After discussing about concepts of ARF-based imaging, ARFI and SWE will be explained in details in Section 3.1 and Sections 3.2, respectively. SWE is the main focus of this thesis and is discussed in more details. Afterward, in Sections 3.3, I review a few well-known methods in displacement estimation with showing some results obtained using those methods. Then I do the same review but in elasticity estimation. In fact Section 3.4 mentions a few results with description of the well-known methods in elasticity estimation. After a review on previous work in this field, I talked about unsolved problems in Section 3.5 and how our proposed methods will resolve these issues. At the end, a summary of the chapter is provided in Section 3.6.

Acoustic radiation force-based (ARF-based) elastography which includes both ARFI and SWE, generates a deep "push" in the tissue by utilizing a non-invasive focused acoustic radiation force (ARF) to a focal point in the tissue Bamber et al. (2013); Bercoff et al. (2002); Catheline et al. (1999); Gennisson et al. (2013); Nightingale et al. (2003); Sandrin et al. (2002); Sarvazyan et al.

(1998) in order to deform tissue and subsequently track the deformation for estimating tissue elasticity E, both quantitatively and qualitatively. Mathematically, the force generated by acoustic radiation in soft tissue is expressed as

$$F = \frac{2\alpha I}{c}, \tag{1}$$

where I denotes the temporal average intensity at a given point in space, α is the absorption coefficient of the medium, and c the speed of sound. For a given region of excitation (ROE), the radiation force is uniform if all three parameters $\{I, \alpha, c\}$ are relatively constant across the ROE. Alternatively, variations in these parameters represent the inhomogeneity in the medium and can be used to derive the mechanical properties of the tissue.

Tissue response to the ARF can be monitored using the ultrasound RF data collected immediately before and after the ARF excitation. Depending on where the resulting disturbance is monitored, two imaging approaches are proposed Nightingale (2011): 1) Acoustic radiation force impulse (ARFI) imaging, wherein tissue deformation is tracked within the ROE. 2) Shear wave elastography (SWE), which unlike ARFI monitors the tissue response away from the ROE to quantitatively estimate the tissue properties from the estimated shear-wave speed (SWS) Bercoff et al. (2002); Nightingale et al. (2001); Sandrin et al. (2002). In this work, our focus is primarily on SWE.

3.1 Acoustic Radiation Force Impulse (ARFI) Imaging

In order to generate ARFI images, both localized and impulsive acoustic radiation force impulsed is needed and a single ultrasound probe is responsible to both transmit acoustic wave and track the deformation Nightingale et al. (2001). In fact, an ARFI pulse has both pushing and tracking information. Commercial ultrasound scanners are able to focus in a specific location within the Region Of Interest (ROI) and transmit acoustic wave inside the tissue and at the same time track the perturbation in the ROI. ARFI imaging starts pushing and imaging the tissue in a specific lateral position using a sequence which consists of three pulse types: 1) Reference pulse which establishes the base-line tissue position before an excitation; 2) excitation pulse which is used to push the tissue locally in order to create a deformation in the ROI; and 3) monitoring pulse which is used right

after the excitation to track the deformation that excitation pulse creates Doherty et al. (2013). This process can be applied across the aperture to result in a 2-D image. Now, using a displacement tracking method, displacement profile can be estimated from reference pulse and all other tracking pulses which the results in displacement filed as a function of time which is suitable to reconstruct physical properties of the tissue using the idea that soft tissue take longer time to reach displacement peak. During the past years, ARFI imaging has shown its potential to investigate stiffness of tissue in vascular and cardiac tissues Hsu et al. (2007,0). In the field of cancer detection, ARFI imaging is highly applied in detection of characterization of the breast Sharma et al. (2004), prostate Zhai et al. (2010) and liver Fahey et al. (2007).

3.2 Shear-Wave Elastography (SWE)

In SWE, a localized and focused radiation force F is applied to the ROE to induce a shear-wave that travels away from the ROE within the region of interest (ROI). During the propagation phase, the displacement field and associated attenuation of the propagating wave contain useful information about the local mechanical properties of the tissue. The displacement field in the tissue is often tracked by high frame rate imaging by exploiting plane-wave imaging Bercoff et al. (2002); Sumi (2005). By comparing frames following the excitation to the reference frame (imaged when the tissue is at rest), the tissue displacement profile or alternatively the propagation velocity of the shear-wave can be determined in both spatial and temporal domains Doherty et al. (2013); Gennisson et al. (2013); Nightingale (2011); Sarvazyan et al. (1998). In an elastic isotropic medium, the relationship between the shear modulus and wave propagation speed is given by the expression

$$c_T = \sqrt{\frac{\mu}{\rho}}, \tag{2}$$

where c_T, μ and ρ represent the propagation speed, tissue shear modulus and tissue density, respectively. This means, estimating velocity of of wavefront traveling inside the tissue while having the tissue density results in shear modulus of the tissue which relatively relates to the stiffness of the tissue. Now, first step will be estimating accurate displacement field which then can be reliable enough for speed estimation. Second step will be using displacement data to extract speed of the

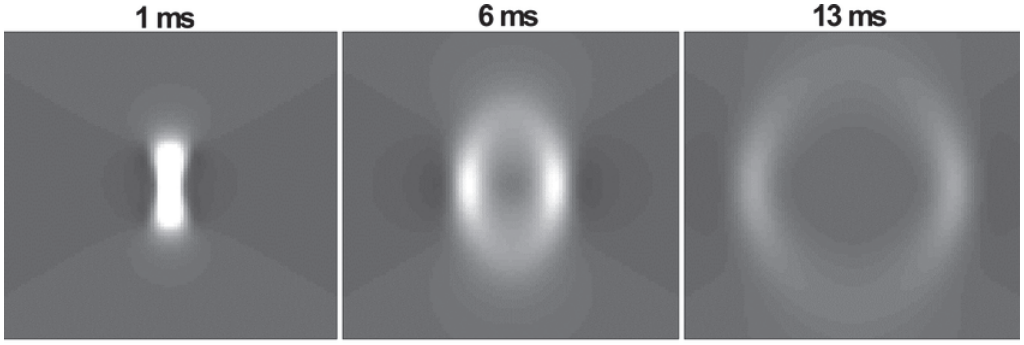

Figure 3.1: Shear wave displacement following the excitation using NCC method in Bercoff *et al.* (2004). This image is from Bercoff et al. (2004).

wave. Two well-known methods are discussed in 3.4 for elasticity estimation.

3.3 Common Approaches for Estimating Displacement

Correlation-based methods Friedrich-Rust et al. (2009); Palmeri et al. (2006); Walker and Trahey (1994) are commonly used for displacement estimation. Due to ease of implementation, even on commercial machine, correlation-based methods are implemented. A very good example for a method which use NCC on shear-wave data is Bercoff et al. (2004). Using a 75% window overlapping NCC, Fig. 3.1 shows obtained result of the paper following the excitation.

As another very strong work, Dumont and Byram (2016) proposed Bayesian estimator to track small displacements in ARFI Imaging. Results of this paper illustrate the superiority of Bayesian approach over NCC. To show robustness of the method against noise, two level of noise is added. In Fig. 3.2 which show 2-D ARFI displacement, both rows are the same unless the level of added noise. From left to right, plots (a)-(f) represent mean NCC results from 25 samples, NCC, NCC with median filter, previous Bayesian estimator proposed by the same author, proposed Bayesian estimator with p=1.05, and proposed Bayesian estimator with p=2. P is a parameter in the formulation which can take different values.

Both NCC and Bayesian methods have disadvantages. NCC takes long time for running and Bayesian is also not suitable for real-time implementation although higher accuracy of that compared to NCC is considerable. In both ARFI and SWE, the goal is to find elasticity map. Therefore,

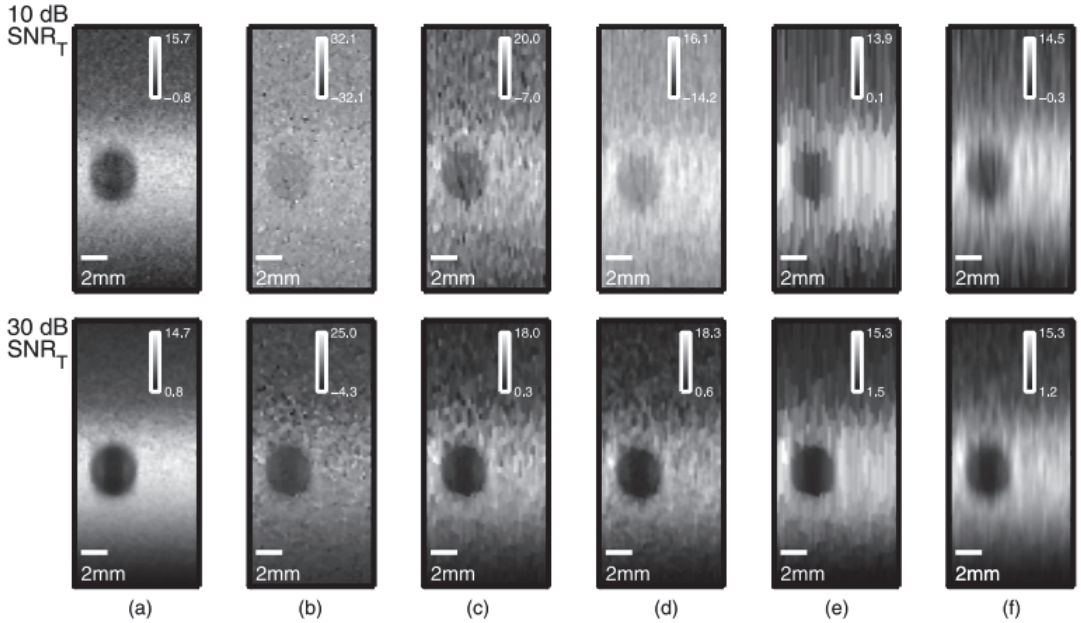

Figure 3.2: 2-D ARFI displacement Bayesian method in Dumont *et al*. (2016) compared to NCC. This image is taken from Dumont and Byram (2016)

in the following section, I study a few work done to reconstruct shear modulus (which is 1/3 elasticity in soft tissue) from displacement field.

3.4 Common Approaches for Estimating Elasticity

Recently, numerous advances have been made in recovering the shear modulus from the displacement fields Bercoff et al. (2004); Carrascal et al. (2017); Fink and Tanter (2011); Lee et al. (2015); Nightingale et al. (2003); Sarvazyan et al. (1998). Among many proposed methods, two methods are more strong than other methods and result in more precise elasticity maps. These two methods are 1) Helmhotz Equation inversion-based approach; and 2) Time of Flight (TOF) Approach; that I will explain both providing result of successful work.

3.4.1 Helmhotz Equation inversion-based approach

The algebraic inversion of the Helmholtz equation has been successfully applied in MR elastography Honarvar et al. (2017); Oliphant et al. (2001); Sinkus et al. (2005); Van Houten et al.

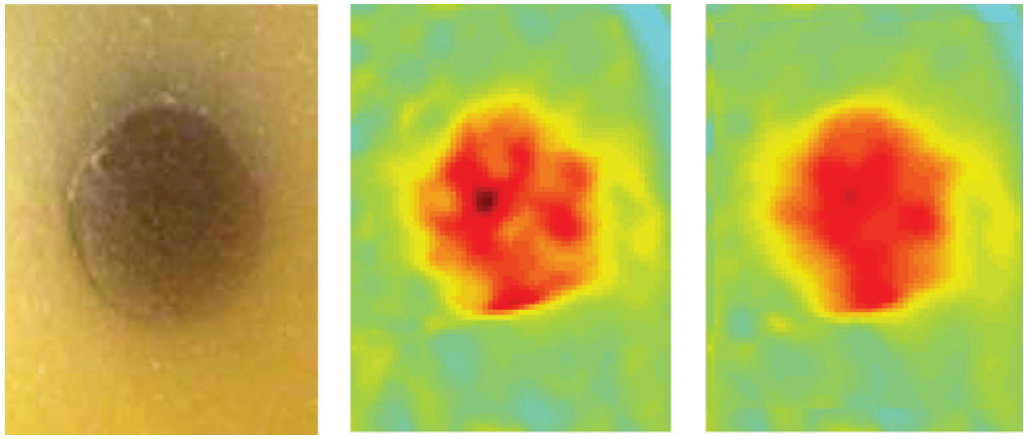

Figure 3.3: Elasticity map of a phantom with lesion implemented by Bercoff *et al*. (2004) paper. As visible, elasticity of the lesion is higher that background. This image is from Bercoff et al. (2004).

(2003). However, this technique has achieved limited success in ultrasound elastography since it involves second-order derivatives and 3D displacement estimates Bercoff et al. (2004); Honarvar et al. (2016); Nightingale et al. (2003); Sandrin et al. (2002). As a good sample, Bercoff et al. (2004) using inversion of Helmhotz equation which refers to wave equation in the tissue, reconstructed elasticity map which is shown in Fig. 3.3.

3.4.2 Time of Flight (TOF) Approach

As a very well-known technique in measuring shear-wave speed and then elasticity, TOF method was proposed and developed during the past years Fink and Tanter (2011); McLaughlin and Renzi (2006a,0); Palmeri et al. (2008); Tanter et al. (2008); Wang et al. (2010). Estimation of the SWS is a common approach, which entails calculating the wavefront arrival time at different lateral positions. (i.e., time-of-flight (TOF))

Fig. 3.4 shows Time to Peak (TTP) in ARFI imaging proposed by Dumont and Byram (2016). In fact, every pixel of these images, indicate the required time for that pixel to meet the maximum of displacement. Time and distance are enough for speed calculation and therefore to find elasticity.

Using shear-wave data, Palmeri et al. (2008) calculated shear modulus using NCC as the displacement estimation method and TOF for elasticity calculation. Fig. 3.5 depicts TTP and reconstructed shear modulus in tissue-mimicking phantom.

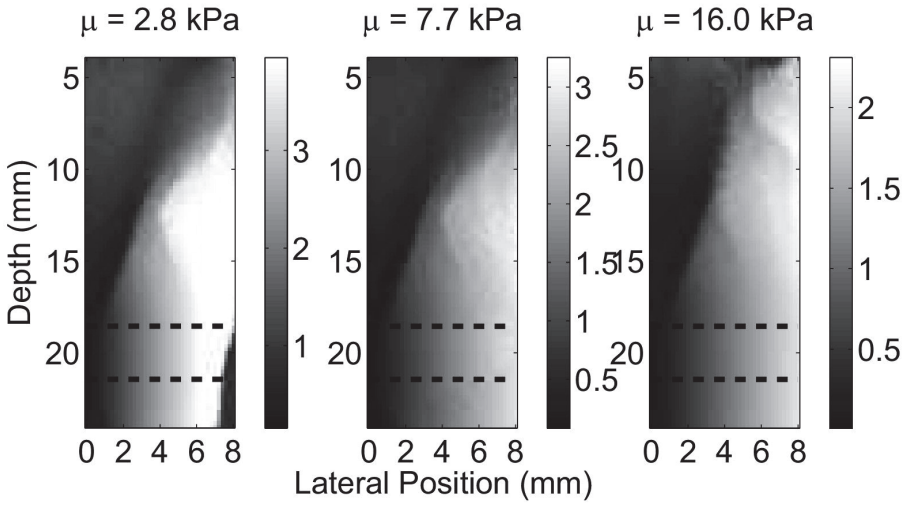

Figure 3.4: Time to peak displacement in Dumont *et al.* (2016) for ARFI imaging. This image is taken from Dumont and Byram (2016).

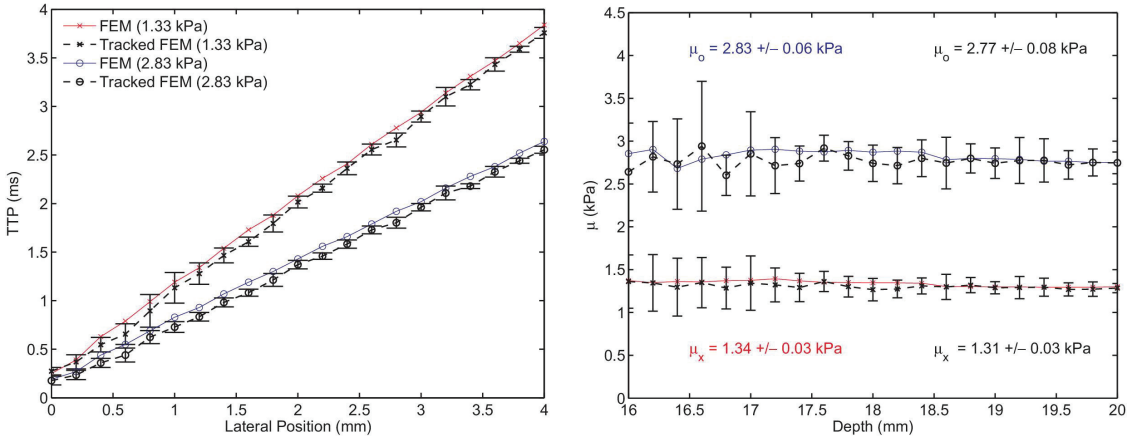

(a) TTP at Focal Depth (b) Reconstructed Shear Moduli

Figure 3.5: Time to peak displacement and shear modulus reconstructed in M. L. Palmeri *et al.* (2008) paper for shear-wave imaging. This image is from Palmeri et al. (2008).

Both inversion of Helmhotz and TOF, although are successful in some scenarios ,they need a highly accurate estimated displacement. Therefore, to have an accurate map of elasticity, displacement estimation is more important step. Focus of this thesis in on accurate displacement estimation, however, using TOF approach I report elasticity at the end. So to make our goal clear again, I explain the issues we face in shear-wave elastography and I introduce our proposed methods in problem statement section.

3.5 Problem Statement

Both inversion of the Helmholtz equation and estimation of the TOF require an accurate and precise displacement estimation, which is challenging since these displacements are very small and the data is noisy. Several post processing techniques have, therefore, been proposed to limit the effect of incorrect displacement estimates Guo et al. (2015); Rouze et al. (2010); Wang et al. (2010) or generate confidence index in SWE Pellot-Barakat et al. (2015). The development of accurate displacement estimation techniques remains an active field of research. During the past years, many approaches are used to find displacement field which a few of them are discussed in the following.

The correlation-based approaches are commonly used for displacement estimation, wherein RF data is divided into small windows and displacement is estimated by maximizing cross correlation metrics Friedrich-Rust et al. (2009); Palmeri et al. (2006); Walker and Trahey (1994). These methods are computationally efficient and have been widely used for estimating displacement fields in the SWE. However, they may generate incorrect estimates mainly due to insufficient information in the correlation window and have a higher Cramer Rao lower bound (CRLB) implying more mean square error. To address these issues, Byram et al. (2012); McCormick et al. (2011) proposed incorporating knowledge of adjacent displacement estimates into the final estimate of a displacement. In another work, Byram et al. (2013) proposed Bayesian speckle tracking (or Bayesian regularization) to improve the displacement field using $a\ priori$ knowledge of the estimation, and showed that with a simple prior scheme, the CRLB can be surpassed. Dumont and Byram (2016) expanded this work and proposed a Bayesian estimator that uses a generalized-Gaussian Markov Random Field (GGMRF) prior that can automatically adjust the distribution of the prior function. While

this method produces high quality displacement maps, it is not immediately suitable for real-time displacement estimation due to its high computational complexity.

To overcome these limitations and to further improve the accuracy of the displacement estimation, I adopt the dynamic programming analytic minimization (DPAM) framework, originally proposed for quasi-static elastography Rivaz et al. (2008,1), in SWE. A cost function that incorporates RF data and prior information of displacement continuity is optimized to calculate the displacement field. Nonlinear terms in the cost function are linearized using their first order Taylor series approximations to allow for efficient optimization of the cost function.

The thesis seeks to further improve the accuracy of the displacement field estimate over Rivaz et al. (2008,1) by incorporating a higher order Taylor series expansion into the cost function. Since inclusion of these terms makes the optimization problem intractable, I propose a novel approach to substantially reduce the computational complexity. We refer to our method as second-order analytic minimization elastography (SESAME). Incorporating second order derivatives was recently proposed in a short abstract Rivaz (2015) in quasi-static elastography. Both DPAM and SESAME generate high quality displacement maps in real time and are, therefore, suitable for their on-line implementation.

The contributions of this work are twofold. First, I extend the DPAM framework, proposed previously for quasi-static elastography, for the first time in SWE. Second, I introduce SESAME, a novel technique for tracking displacements using RF data. A short version of this paper is published recently in a conference paper Horeh et al. (2017).

3.6 Summary

In this chapter, I presented a literature review of ARF-based elastography under category of dynamic elastography. As two popular methods of ARF-based elastography, I introduced ARFI imaging and SWE. In ARFI imaging, the ultrasound beam excites the tissue and ARFI imaging is interested in tracking displacement along the excitation axis. SWE, unlike ARFI imaging, excites the tissue and then tracks the deformation in neighboring of the excitation point.

As the well-known methods in displacement estimation, I talked about NCC and Bayesian estimators and presented the result of displacement. Bayesian estimator has higher accuracy because it takes advantage of prior information.

Then, inversion of of Helmholtz equation and Time of Flight (TOF) were presented by results of three papers. In inversion of of Helmholtz equation, displacement field is enough for shear modulus estimation although second derivative of displacement considerably amplifies probable noises in the system. In TOF, time which takes for every sample of the image to meet its maximum value is calculated and having the distance, speed of the shear-wave and then shear modulus is reconstructed. Both methods need to receive an accurate displacement field. So estimating displacement is more important. In this thesis, I propose two novel methods based a minimization of a cost function in so that subsample displacement estimation is possible. In next chapter, I explain formulation of the proposed methods for displacement estimation.

Chapter 4

Methodologies for Estimating Displacement

In this chapter, proposed methods of estimating displacement are presented. In Section 4.1, I introduce our implementation of NCC method. NCC is implemented only for comparison. Then in Section 4.2, I describe how our proposed methods are formulated using regularization part. DP and DPAM are also introduced for integer and subsample displacement estimation, respectively. I incorporate more information in DPAM and introduce another estimator in Section 4.3. In Section 4.4, validation is described and Section 4.5 talks about computation complexity of the methods and the chapter ends with a summary.

In SWE, a reference ultrasound frame is initially collected from the tissue. An ARF excites a small region (shown as the yellow ellipse in Fig. 4.1 (a)), which is followed by collecting multiple ultrasound frames as shown in Fig. 4.1 (b) to monitor the propagation of the shear-wave. The reference frame is collected before applying the ARF, while the remaining frames are collected during the wave propagation phase.

Let $I_1(i,j)$ and $I_2(i,j)$ be two ultrasound frames prior to and during deformation as shown in Fig. 4.1 (c)-(d). Symbol I denotes the intensity of a discretized sample of the RF signal with $i = 1, \cdots, m$ and $j = 1, \cdots, n$ representing respectively the axial (z) and lateral (x) locations of the pixel. The goal of the tracking method is to find two matrices A and L such that their $(i,j)^{\text{th}}$

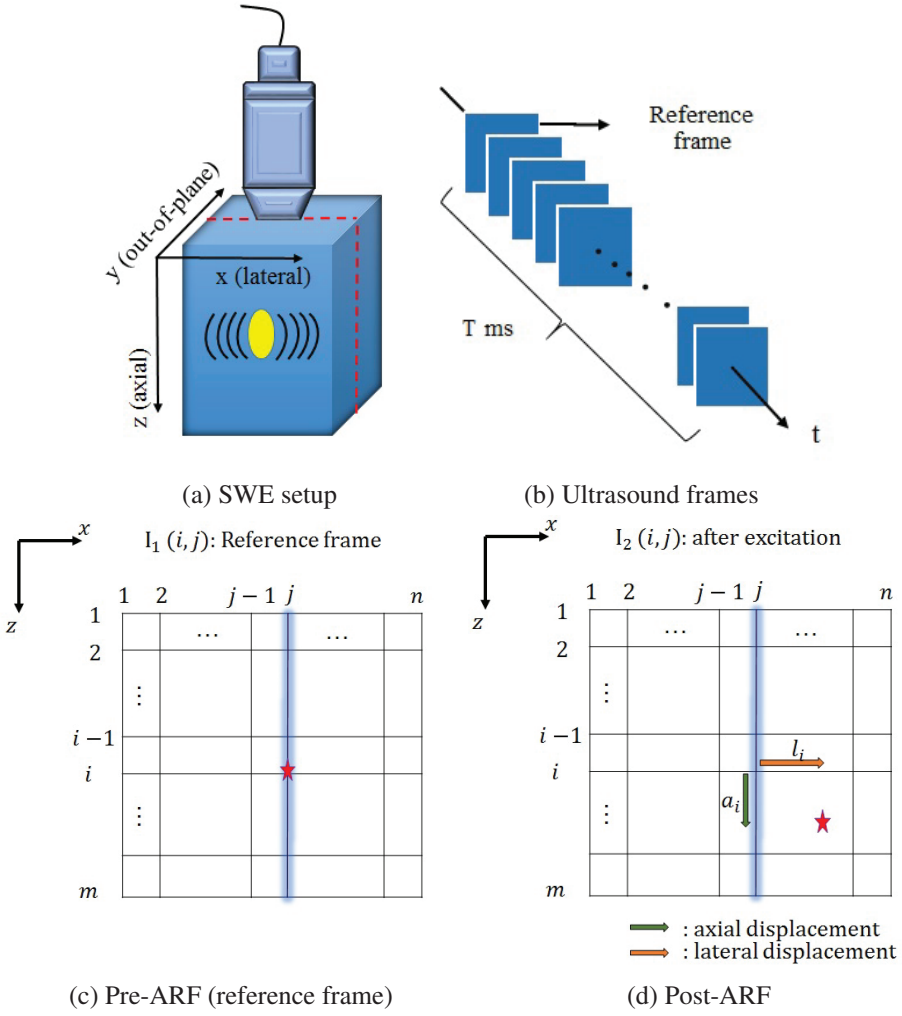

(a) SWE setup (b) Ultrasound frames

(c) Pre-ARF (reference frame) (d) Post-ARF

Figure 4.1: Schematics of SWE. In (a), ARF generates excitation in the ROE (shown as a yellow ellipse) resulting in the propagation of shear-waves from the ROE to the sides. The reference tissue is imaged at the cross section specified by red dashed lines in (a), which generates a sequence of ultrasound images shown in (b). To track the associated wave propagation, displacements for sample (i, j) (marked by a red star in (c)) in the reference frame are calculated by matching it with its corresponding point (marked by another red star in (d)).

elements, i.e., $a(i,j) \in A$ and $l(i,j) \in L$ provide estimates of the axial and lateral displacement for pixel (i,j). Note that the traditional window-based techniques calculate displacement for each window, whereas our goal is to estimate displacement for each pixel.

In order to estimate displacement field between two RF frames, two proposed approaches are discussed in the following. Moreover, a very well-known correlation-based known as Normalized Cross Correlation (NCC) is also discussed. The reason is that, I always tend to compare our results to basic methods to show the superiority of the proposed methods. Therefore, in the following section, I first talk about how NCC is implemented and then DPAM and SESAME methods are explained afterward.

4.1 Correlation-based Estimation

The correlation-based approaches are commonly used for displacement estimation, wherein RF data is divided into small windows and displacement is estimated by maximizing cross correlation metrics Friedrich-Rust et al. (2009); Palmeri et al. (2006); Walker and Trahey (1994). In this work, I apply the NCC using the following formulation to calculate NCC value between two signals:

$$c(n) = G(m) \otimes S(n) = \frac{1}{N\sigma_G\sigma_S} \sum_{m=0}^{N} G(m)S(m-n) \tag{3}$$

where σ_G and σ_S are the RMS deviations:

$$\sigma_G^2 = \frac{1}{N} \sum_{n=0}^{N} G(n)^2 \tag{4}$$

$$\sigma_S^2 = \frac{1}{N} \sum_{n=0}^{N} S(n)^2 \tag{5}$$

where $G(m)$ and $S(n)$ refer to two corresponding windows in two images, pre and post deformation, respectively. In addition, N is the number of pixels lies in the window. The computation procedure is done as following steps:

(1) Starting from the first pixel in pre deformation image and take a window of a specific size

Figure 4.2: Nine NCC values calculated between a fixed window in pre compression and shifted windows in post compression image. NCC_{ij} means the window in post compression image is shifted i samples in lateral direction and j samples in axial direction. This enables us to fitting a polynomial using 9 nodes and find the real maximum which indicates exact values of axial and lateral displacement. For every pixel, this matrix should be calculated first and then subsample is estimated by curve fitting.

around it and call the windown G.

(2) Choose the corresponding pixel in the post compression image and take the same size of window and call it S.

(3) Using the Eq. 3, NCC value between two patches is calculated.

(4) Window G remains at a fix position but window S moves one pixel up, down, right, left and four corners. At each movement, NCC value is calculated. Since in shear-wave elastography, displacement are in order of micrometer, displacement are always less than a pixel in normal medical images. So at the end nine NCC values are available which creates a 3×3 NCC matrix.

(5) By fitting a polynomial function, maximum value in NCC matrix is estimated which specifies the displacement regarding the pixel picked up in step 1.

(6) For every other pixel, steps 1 to 5 need to repeated so that displacement images will be

estimated.

These methods are computationally efficient and have been widely used for estimating displacement fields in the SWE. However, they may generate incorrect estimates mainly due to insufficient information in the correlation window and have a higher Cramer Rao lower bound (CRLB) implying more mean square error. An alternative to correlation-based methods is regularization-based method which not only is faster, but also use regularization term to include neighboring information and displacement continuity which results in more accurate and smoother displacement images.

4.2 Regularization-based Estimation

In regularization-based approach, to achieve accurate sub-sample displacement field, estimation breaks into two main parts. In the first part, global optimization is performed using DP to estimate displacement for one "seed" RF-line. This is an integer optimization wherein the displacement map is restricted to integer values. In the second part, a local optimization step, DPAM or SESAME, is carried out to generate sub-integer displacement maps. Since the RF data alone can be noisy and insufficient at certain locations for the estimation of the displacement field, I incorporate the prior information of displacement continuity as a regularization term. The combination of global and local optimization, as well as this regularization term, makes our algorithm robust to noise and artifacts in the RF data. Below, the DP, DPAM and SESAME approaches are introduced next.

4.2.1 Dynamic Programming (DP)

To describe the DP formulation Bellman and Dreyfus (2015), I consider a single column j (RF-line j) of the image $I_1(i,j)$ prior to excitation as highlighted with blue color in Fig. 4.1 (c)-(d). For sample i, I denote the axial and lateral displacements by $\{a_i, l_i\}$. The prior information (referred to as the regularization term) is

$$R(a_i, l_i, a_{i-1}, l_{i-1}) = \alpha_a (a_i - a_{i-1})^2 + \alpha_l (l_i - l_{i-1})^2, \tag{6}$$

which restricts displacements $\{a_i, l_i\}$ of sample i to values close to the displacements $\{a_{i-1}, l_{i-1}\}$ of the previous sample $i-1$. Symbols $\{\alpha_a, \alpha_l\}$ are axial and lateral regularization weights. For column j, the regularized cost function in DP is recursively formulated as

$$C_j^{(p)}(a_i, l_i, i) = \big[I_1(i,j) - I_2(i+a_i, j+l_i)\big]^2 + \min_{d_a, d_l} \Big[\frac{C_j^{(p)}(d_a, d_l, i\text{–}1) + C_{j-1}^{(p)}(d_a, d_l, i)}{2} + R(a_i, l_i, a_{i-1}, l_{i-1})\Big] \tag{7}$$

where superscript p refers to the estimated pixel displacements (as opposed to sub-pixel/subsample estimates) and $\{d_a, d_l\}$ are the optimization parameters corresponding to axial and lateral displacements used to minimize the term within the bracket. Likewise, terms a_i, l_i, d_a and d_l denote integer displacements. After calculating $C_j^{(p)}$, for $i = 2, \cdots, m$, the cost function is minimized at $i = m$ with respect to integer values for a_m and l_m for all samples of the j^{th} line.

4.2.2 Dynamic Programming Analytic Minimization (DPAM)

Given the foregoing DP axial and lateral displacement estimates $\{a_i, l_i\}$, our goal is to find Δa_i and Δl_i such that $(a_i + \Delta a_i,\, l_i + \Delta l_i)$ are subsample values of axial and lateral displacements. I define a regularized cost function

$$\begin{aligned} C_j^{(s)}(\Delta a_1, \cdots, \Delta a_m, \Delta l_1, \cdots, \Delta l_m) = & \\ \sum_{i=1}^{m} \Big\{ & [I_1(i,j) - I_2(i + a_i + \Delta a_i, j + l_i + \Delta l_i)]^2 \\ & + \alpha(a_i + \Delta a_i - a_{i-1} - \Delta a_{i-1})^2 + \beta_a(l_i + \Delta l_i - l_{i-1} - \Delta l_{i-1})^2 \\ & + \beta_l'(l_i + \Delta l_i - l_{i,j-1})^2 \Big\}, \end{aligned} \tag{8}$$

where superscript s refers to subsample cost function and $\{\alpha, \beta_a, \beta_l'\}$ are regularization weights. To simplify the notation, I have dropped the index j in terms a_i and l_i in Eq. (8). In other words a_i, l_i, Δa_i and Δl_i represent the displacements of sample (i, j). Symbol $l_{i,j-1}$ is the lateral displacement of the previous RF-line. Note that $l_{i,j-1}$ denotes the total lateral displacement of the previous line, i.e., when the displacement of the $(j-1)^{\text{th}}$ line was calculated, $l_{i,j-1}$ was updated with $l_{i,j-1} +$

$\Delta l_{i,j-1}$. Eq. (8) is nonlinear because the variables Δa and Δl appear inside the nonlinear function I_2. In addition, typical RF data contains around $m = 2000$ samples per line, leading to 4000 unknowns in Eq. (8) (taking into account the axial and lateral displacements for each sample). Consequently, the optimization of the cost function in Eq. (8) is intractable. Rivaz et al. (2014) proposed to approximate the summation term in Eq. (8) involving I_2 with the following first order Taylor series expansion

$$I_2(i + a_i + \Delta a_i, j + l_i + \Delta l_i) \approx \\ I_2(i + a_i, j + l_i) + \Delta a_i I'_{2,a} + \Delta l_i I'_{2,l}, \tag{9}$$

where $I'_{2,a}$ and $I'_{2,l}$ are, respectively, the axial and lateral derivatives of I_2. Substituting the above expression in Eq. (8) results in a quadratic equation, which can then be converted into a linear system of equations by setting its partial derivatives with respect to the optimization variables equal to zero. The linear system of equations has a sparse coefficient matrix, which can be exploited to solve the system in real time on a typical desktop computer Rivaz et al. (2014).

4.3 2nd Order Analytical Minimization Elastography (SESAME)

The omission of higher order terms in the Taylor series expansion makes Eq. (9) less accurate, whereas inclusion of higher order terms renders the cost function intractable. In this section, I propose to include information from the second order term of the Taylor series expansion while keeping the optimization problem tractable. The outline of our algorithm is presented in Algorithm 1.

The second order Taylor series expansion of term $I_2(i + a_i + \Delta a_i, j + l_i + \Delta l_i)$ in Eq. (8) contains Δa_i^2 and Δl_i^2. Substituting these terms into Eq. (8), on one hand, results in a polynomial cost function of order 4. On the other hand, for an RF data of length 2000, Eq. (8) has 4000 variables. Optimization of such a high dimensional nonlinear cost function is intractable. Instead of directly incorporating the second-order Taylor series term, I propose to penalize samples where

Algorithm 1 SESAME

procedure SESAME ($A(i,j),\ L(i,j)$)
    Pick a "seed" RF line for DP
    $a_i \leftarrow$ Integer axial Disp. using DP
    $l_i \leftarrow$ Integer lateral Disp. using DP
    Linear interpolation of the integer values
    Δa_i & $\Delta l_i \leftarrow$ SESAME
    for <all RF lines> **do**
        Δa_i & $\Delta l_i \leftarrow$ SESAME
    end for
    repeat 6 for the other lines
end procedure

this term is large and the first-order Taylor expansion is not accurate. The revised cost function is

$$
\begin{aligned}
&C_j^{(s)}(\Delta a_1, \cdots, \Delta a_m, \Delta l_1, \cdots, \Delta l_m) = \qquad (10)\\
&\sum_{i=1}^{m} \Big\{ w_{i,j}[I_1(i,j) - I_2(i + a_i + \Delta a_i, j + l_i + \Delta l_i)]^2 \\
&+\alpha(a_i + \Delta a_i - a_{i-1} - \Delta a_{i-1})^2 + \beta_a(l_i + \Delta l_i - l_{i-1} - \Delta l_{i-1})^2 \\
&+\beta_l(l_i + \Delta l_i - l_{i,j-1})^2 \Big\}, \\
&\text{where} \qquad w_{i,j} = \frac{1}{\epsilon + |I''_{2,a}(i,j)| + |I''_{2,l}(i,j)|}, \qquad (11)
\end{aligned}
$$

and ϵ a small positive constant to prevent the denominator from becoming zero. Symbols $|I''_{2,a}(i,j)|$ and $|I''_{2,l}(i,j)|$ denote the absolute values of the second-order derivatives of the intensities in the axial and lateral directions respectively. Intuitively speaking, incorporation of $w_{i,j}$ in the cost function penalizes samples that have a high curvature and, therefore, cannot be linearized.

If the displacement estimates associated with the previous line are inaccurate, they will affect the displacements of the next line through the last term in the right hand side of Eq. (10). I avoid propagating this error to the neighboring RF lines by replacing β_l with

$$\beta_l^{(1)} = \frac{\beta_l}{1 + |r_{i,j-1}|}, \qquad (12)$$

where $r_{i,j-1}$ is the residual associated with the displacement of sample i of the previous line. When there is a large residual, $\beta_l^{(1)}$ will be small and its influence on the next line is reduced.

The optimal (Δa_i,Δl_i) values will make the partial derivatives of C_j with respect to Δa_i and Δl_i equal to zero. Setting $\partial C_j/\partial \Delta a_i = 0$ and $\partial C_j/\partial \Delta l_i = 0$, for $i = 1 \cdots m$, and stacking the $2m$ unknowns in $\Delta d = [\Delta a_1, \Delta l_1, \Delta a_2, \Delta l_2, \cdots, \Delta a_m, \Delta l_m]^T$ and $2m$ initial estimates in $d = [a_1, l_1, a_2, l_2, \cdots, a_m, l_m]^T$ results in the matrix-vector representation

$$\underbrace{(\mathbf{I_2'^2} + \mathbf{D_1} + \mathbf{D_2})}_{\mathbf{A}} \mathbf{\Delta d} = \underbrace{\mathbf{I_2'e} - \mathbf{D_1 d}}_{\mathbf{B}} \tag{13}$$

where $\mathbf{I_2'^2} = \text{diag}[\mathbf{J'^2}(\mathbf{1}) \cdots \mathbf{J'^2}(\mathbf{m})]$ is a symmetric tridiagonal matrix of size $(2m \times 2m)$ with

$$\mathbf{J'^2}(\mathbf{i}) = \begin{bmatrix} I_{2,a}'^2 & I_{2,a}' I_{2,l}' \\ I_{2,a}' I_{2,l}' & I_{2,l}'^2 \end{bmatrix} \tag{14}$$

blocks on its diagonal entries where $I_{2,a}'$ and $I_{2,l}'$ are the derivatives of I_2 at point $(i + a_i, j + l_i)$ in the axial and lateral directions,

$$\mathbf{D_1} = \begin{bmatrix} \alpha & 0 & -\alpha & 0 & 0 & 0 & \cdots & 0 \\ 0 & \beta_\alpha & 0 & -\beta_\alpha & 0 & 0 & \cdots & 0 \\ -\alpha & 0 & 2\alpha & 0 & -\alpha & 0 & \cdots & 0 \\ 0 & -\beta_\alpha & 0 & 2\beta_\alpha & 0 & -\beta_\alpha & \cdots & 0 \\ 0 & 0 & -\alpha & 0 & 2\alpha & 0 & \cdots & 0 \\ \vdots & & & & & & \ddots & \\ 0 & 0 & 0 & \cdots & -\alpha & 0 & \alpha & 0 \\ 0 & 0 & 0 & \cdots & 0 & -\beta_\alpha & 0 & \beta_\alpha \end{bmatrix}, \tag{15}$$

and $\mathbf{D_2} = \text{diag}(\mathbf{0}, \beta_\mathbf{l}', \mathbf{0}, \beta_\mathbf{l}', \cdots, \mathbf{0}, \beta_\mathbf{l}')$ is a diagonal matrix with dimensions $(2m \times 2m)$. Similarly, matrix $\mathbf{I_2'}$ is diagonal with the structure

$$\mathbf{I_2'} = w_{i,j} \times \tag{16}$$
$$\text{diag}(I_{2,a}'(1), I_{2,l}'(1), I_{2,a}'(2), I_{2,l}'(2), \cdots I_{2,a}'(m), I_{2,l}'(m))$$

Table 4.1: Parameters for the ARF simulations.

Probe Parameters	Value
Center freq	3 MHz
Samp. freq	30 MHz
element height	14 mm
Element pitch	0.477 mm
Speed-of-sound	1540 m/s
Frac. bandwidth	100%
Elevation focus	50 mm
No. of elemets	128
Active elements	64

where $I'_{2,a}(i)$ and $I'_{2,l}(i)$ are calculated at site $(i + a_i, j + l_i)$ and $\mathbf{e} = [e_1 e_1 \cdots e_m e_m]^T$ with $e_i = w_{i,j}(I_1(i,j) - I_2(i + a_i, j + l_i))$. Having $\mathbf{\Delta d} = [\mathbf{\Delta a_1}, \mathbf{\Delta l_1}, \mathbf{\Delta a_2}, \mathbf{\Delta l_2}, \cdots, \mathbf{\Delta a_m}, \mathbf{\Delta l_m}]^\mathbf{T}$ and $2m$ initial estimates in $\mathbf{d} = [\mathbf{a_1}, \mathbf{l_1}, \mathbf{a_2}, \mathbf{l_2}, \cdots, \mathbf{a_m}, \mathbf{l_m}]$, I will find the $2m$ axial and lateral displacements for $i = 1 \cdots m$ for line j. Afterwards, I follow the same procedure for the neighboring line and consider the calculated displacement on line j as its initial value. Repeating this algorithm gives us both axial and lateral displacement values for the entire image.

4.4 Validation

I compare NCC, DPAM and SESAME using both simulated and real data. In the following I explain how data are acquired for validation in both scenarios, respectively:

(1) Simulation Data:

Simulation data was used to assess the precision and accuracy of both DPAM and SESAME approaches. The probe specifications are listed in Table 4.1. In order to model the tissue, a uniform phantom of dimension $(100 \times 50 \times 20)$ mm in axial, lateral and out-of-plane directions, respectively, with a constant attenuation coefficient of 0.45 dB/MHz/cm is considered. A minimum of 11 scatterers per resolution cell Palmeri et al. (2006); Rivaz et al. (2006) are uniformly distributed in the phantom with Gaussian scattering strengths Wagner et al. (1983). Field II software Jensen (1996) is used for the ultrasound simulation as is the case in Palmeri

et al. (2005). The finite element ground-truth displacement fields for shear-wave propagation are provided by Quantitative Imaging Biomarkers Alliance (QIBA) Palmeri and Qiang (2016); Palmeri et al. (2017). For each scatterer, the displacement is computed by interpolating the displacements of its neighboring nodes using bilinear interpolation. The second image is generated after displacing all scatterers using Field II software. Field II performance is explained by more details in Appendix A. This procedure is repeated such that n total images are simulated during shear-wave propagation. All simulations are repeated for point shear-wave excitation at three different focal depths of 30, 50, and 70mm, and for four different mediums having shear modulus of 1, 2, 5 and 10KPa respectively. In addition, 25 independent speckle realizations were generated in all configurations using Field II. Therefore, not only displacement and elasticity estimation will be possible, but also 25 samples will allow us to report the mean and variance to illustrate performance of the proposed methods and show how the proposed methods outperform NCC in both more accurate displacement estimation and less deviation yielded.

(2) Real Data:

For testing the developed algorithms and compare with NCC, real data are acquired from ultrasound machine in PERFORM CENTRE, Montreal, Quebec, Canada. As a medium under imaging, a custom-made CIRS phantom (Norfolk, VA) with Young's modulus of 7KPa in the background including two lesions with different elasticities and material density of 1.03g/cm^3 is used in our studies. Exact parameters regarding all the regions in the phantom is presented in Table 4.2. An Alpinion ECUBE R12 ultrasound machine (Bothell, WA) and an L3-8 transducer were used for data collection. The probe is a linear array probe with capability of shear-wave data collection with high frame-rates. Fig. 4.3 has three points which should be noted. 1) CIRS phantom; 2) L3-8 transducer; and 3) is a very important point that the probe is hand-held during the data collection phase. Results obtained in this step, determine that the noise added by probable hand shaking is canceled out and results are still precise enough. In order to do the experiment well, suitable parameters are set in the ultrasound setting to excite the medium and track the deformation well. The associated ARF parameters

Figure 4.3: Setup for phantom studies: The probe is hand-held during data collection from a CIRS elastography phantom. An excitation with period of 160μs at the focal depth of 20mm is applied as ARF and a set of 80 RF frames were acquired to monitor the shear-wave.

are listed in Table 4.3. The focus point of the imaging ultrasound is at a depth of 20mm and the excitation frequency is 8MHz. The collected RF data frames are of size 4cm (416 samples) in the axial (depth) direction and 3.81cm (128 samples) in the lateral (width) direction. Due to poor lateral resolution of ultrasound images (caused partly by the large pitch of the L3-8 transducer), up-sampling by a factor of 3 in the lateral direction is performed for all methods. This is limited to experimental data, and no up-sampling is performed for the simulated data. The SWS and shear modulus are related according to Eq. (2), which is used to estimate the shear modulus from SWS. As mentioned previously, the phantom is a 3-D volume which includes three regions as shown in Fig. 4.4.

Background, lesion 1, and lesion 2 are depicted with three colors of green, blue and purple, respectively. The elasticity of these three regions are also 7KPa, 21KPa, and 45KPa. These

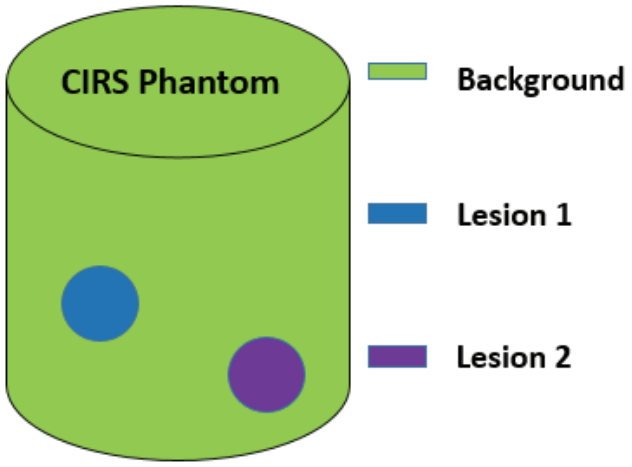

Figure 4.4: Setup of real phantom used for real experiments. As shown, the phantom includes three region. Background , lesion 1 and lesion 2 specified with three different colors. In term of elasticity, background has the smallest and lesion 2 has the greatest elasticity modulus which is referred to stiffness of the medium.

Table 4.2: Parameters for the custom shear-wave phantom with lesions.

	Young's modulus (KPa)	Speed of Sound (m/s)	Attenuation Coefficiend (dB/cm/MHz)
Background	7	1535	0.53
Lesion 1	21	1545	0.52
Lesion 2	45	1562	0.47

Table 4.3: Parameters for the real phantom experiments.

Probe Parameters	Value
Excitation pulse length	160 μs
Aperture size	64
Samp. freq. (f_c)	40 MHz
PRF	60 KHz
Element pitch	0.3 mm
Excitation focal depth	2 cm

numbers indicate that lesion 2 is stiffer that lesion 1 and both lesions are stiffer than background. In fact, these lesions treat as tumors in the body treat. In order to assess strength of the proposed methods in comparison with NCC, two scenarios are considered. 1) In a uniform medium which no lesion is available; 2) in presence of lesion which models tumor in body.

Normalized cross correlation (NCC) with a window-size of (70×10) samples and 98% kernel

overlap with 2-dimensional parabolic interpolation for estimation of subsample displacements was used for comparison. For quantitatively comparison, the SNR is calculated using the following equations Dumont et al. (2016)

$$\text{SNR} = \frac{\mu^2}{\text{MSE}} \quad \text{and} \quad \text{MSE} = E[(d_e - \bar{d})^2], \tag{17}$$

where μ is the mean displacement value at a specific axial location on the excitation trajectory averaged over all the realizations, MSE denotes mean square error, and $\{d_e, \bar{d}\}$ are, respectively, the estimated and ground truth displacement fields.

4.5 Computational Complexity

To achieve a better understanding of complexity of the proposed methods in this work (DPAM, SESAME) and also NCC, complexity of every methods is separately discussed in the following by providing computational operations needed for getting a result as supposed the displacement image.

- Normalized Cross Correlation (NCC):

  Computational cost in NCC depends on the number of RF lines in RF image, number of windows, and cost of calculating NCC in every window. For a single RF line, computation is considered as C_{NCC} as below:

  $$C_{NCC} = N_w \times N_{iter} \times C_{iter}, \tag{18}$$

  where N_w is the number of windows in a single RF line, N_{iter} refers to number of iterations in every window, and C_{iter} is the cost of every iteration. N_{iter} depends on the maximum displacement I expect. For instance, in quasi-static elastography, compression applied to the tissue, depending on the application, from 1% to 10% or even more compresses the tissue. Therefore, in a normal RF image of size 1000 in axial direction, maximum displacement of 10 pixels in 1% compression is expected. In shear-wave elastography, since displacements are in order of micrometer (maximum 20 μm), maximum one pixel displacement is considered to

shift the window in post excitation images. Because of displacement in the lateral direction as well as axial, the window should also shifted in lateral direction such that lateral displacement to be calculated. This not only enable us to calculate lateral displacement, but also helps us to estimation axial displacement more precisely. C_{iter} in terms of (add, multiplications) considering the Eq. (**??**), is almost ($5\times W_L$, $3\times W_L$) where W_L is the length of window. In this work, W_L is considered 70 and 10 samples in axial and lateral directions respectively in an image of size (1388 (axial) $\times$ 150 (lateral)). Obviously, the cost of every RF line should be multiplied by the number of RF lines in RF data to find the cost of NCC method for displacement estimation. In this study, in simulation data, 150 RF lines are considered while in real data, this values reduces to 128.

- DPAM and SESAME:

  On a related note, I observe Eq. (13) contains diagonal matrices ($\mathbf{D_2}, \mathbf{\Delta d}, \mathbf{I_2'}, \mathbf{d}$), tridiagonal matrix $\mathbf{I_2'^2}$), and pentagonal matrix $\mathbf{D_1}$. Using notations $\mathbf{A}$ and $\mathbf{B}$ in (13), the equation is formulated as $\mathbf{A\Delta d} = \mathbf{B}$, which can be efficiently solved since $\mathbf{A}$ is highly sparse. More specifically, Eq. (13) can be solved for $\mathbf{\Delta d}$ in $9m$ operations since the coefficient matrix $\mathbf{A}$ is pentadiagonal and symmetric. In fact, due to being symmetric, $(I_2'^2 + D_1 + D_2)$ term is to be solved in $9m/2$ operations because the matrix $\mathbf{A}$ is symmetric. On the other hand, solving a full linear system of simultaneous equations of size $2m$ is $(2m)^3/3$ which is substantially greater than $9m/2$. The same result in terms of computational complexity is obtained using DPAM as shown in Rivaz et al. (2011). The main difference between computation of DPAM and SESAME is calculating second order derivative of the image of size $2m$ in SESAME which results in additional $2m$ equations to be solved as compared to DPAM. But considering the additional computation, the number of operations due to sparsity of the matrix is still substantially smaller than $(2m)^3/3$ (operations to solve a full linear system of size $2m$). Although SESAME, compared to DPAM, utilize second order Taylor series term to add more information to the system to yield more accurate displacement estimation, the complexity of that is not much higher as compared to DPAM. Computation time in the following will state how this additional needed operation in SESAME as compared to DPAM affects the

computation time on the same CPU.

The NCC is implemented directly in MATLAB while the DPAM and SESAME algorithms are implemented in C++ as MATLAB Mex functions. An Intel i5-4690 3.50GHz CPU with 16GB of memory is used for signal processing. For the RF data of size (1388×150), NCC, DPAM and SESAME take 42.4, 0.035 and 0.042 seconds, respectively. The NCC window-size is (70×10) samples and the overlap between successive windows is 98%. All reported execution times are calculated based on 150 independent executions of the programs in our Monte Carlo simulations.

4.6 Summary

In this section, first talk about how two images are acquired two calculate displacement between them. In fact, in SWE, a frame before excitation is supposed as pre-ARF (or reference frame) and every frame after excitation is post-ARF image. The goal is to calculate displacement between the reference frame and one post-ARF frame. I then explained how NCC is formulated to represent a correlation-based method for comparison. Afterward, DP and DPAM are introduced which respectively refer to integer and subsample displacement estimation. Furthermore, SESAME as another proposed method is introduced which results in more accurate estimation due to more information it involved in calculation by using higher order of Taylor series. In validation section, I explained how simulation are simulated using Field II software and and how real data are acquired using ultrasound machine and CIRS phantom. Finally, computation of proposed methods and NCC is discussed. I observed that, SESAME has almost the same complexity as DPAM, however, it considerably improves the results.

Chapter 5

Results

In order to assess the accuracy and precision of the proposed methods and to compare the results with a correlation-based method, we test on both simulation data and real data acquired from an Alpinion ultrasound machine in PERFORM CENTRE, Concordia university, Montreal, Canada. In Section 5.1, first we explain procedure of how simulation data are created and then show superiority of the proposed method by comparing both displacement and elasticity results. Afterward, in Section 5.2, results are obtained using real data collected from an experimental phantom using ultrasound machine. To show the accuracy of the proposed methods, the experiment is done in two scenarios. First, in a uniform phantom without any lesion inside the medium and second experiment is done in presence of lesion as opposed to tumor in the body. Real experiments are done by holding the probe with hand which shows the accuracy and precision of the proposed methods even in presence of any noise caused by holding the ultrasound probe with hand.

5.1 Simulations

In this section, results of simulation phase including displacement field, SNR and elasticity estimation are presented. As explained previously, in this section, experiment is done in the uniform part of the phantom as depicted in Fig. 4.4.

Fig. 5.1 shows the axial displacement field at 4ms following the excitation in the simulation phantom with the shear modulus of 10KPa and focal configuration of F/3.5. The experiment is

done for 3 different excitation focal points, 30 mm, 50 mm and 70mm. The FEM ground truth as well as the NCC, DPAM and SESAME displacement fields are shown for each focal point in a row. Plot (a) represent ground-truth displacement field while plots (b)-(d) show associated estimated displacement field using NCC, DPAM and SESAME methods, respectively. Second row where plots (e)-(h) are depicted, everything is the same as first row unless excitation focal point which is 50 mm. Plots (i)-(l) represent the same experiment but at excitation focal point of 70 mm. The color-bars are displayed in μm and represent the common dynamic range used to plot the displacement frames in each row. In Fig. 5.1, it is clear that both DPAM and SESAME outperform NCC in term of wavefront tracking which is quite significant for accurate SWS calculation. In other words, the more accurate displacement and specifically wavefront tracking is estimated, the more accurate elasticity will be estimated which is exactly referred to hardness of the tissue.

Fig. 5.2 corresponds to axial displacement estimated from a uniform medium with a 10KPa shear modulus excited at the focal depth of 70mm. In plots (a)-(c), displacement is plotted as a function of lateral direction calculated at the same depth as the excitation point in a range of 2-23mm, respectively for three different time instances of 1.5, 4, and 6.5ms following the excitation. Solid lines represent ground-truth displacement, and the blue dotted, red and yellow dashed lines show displacement calculated using NCC, DPAM and SESAME methods, respectively. As clearly is visible, DPAM and SESAME compared to NCC, result in more accurate wavefront tracking which is the key point is elasticity estimation although the accurate estimating of the whole displacement field is significant. Plots (d)-(f) are jitter estimated associated to plots (a)-(c). In fact, every plot in (d)-(f) shows the how proposed methods outperform NCC in terms of less jitter. As observed, both DPAM and SESAME estimators outperform NCC in three aspects: 1) A displacement profile similar to the ground truth; 2) Less underestimation (bias), and; (3) Less jitter.

The SNR values associated with the displacements of the uniform phantom with the shear modulus of 10KPa at the ARF focal depths of 70mm are calculated using Eq. 17 and shown in Fig. 5.3 as a function of time. Error bars represent mean and standard deviation over 25 independent speckle realizations simulated using different random distribution of the scatterers. Since in simulation part of the work, ground truth is given, comparing obtained results with ground truth will result in feasible assessment both qualitatively and quantitatively. Results using the DPAM and SESAME

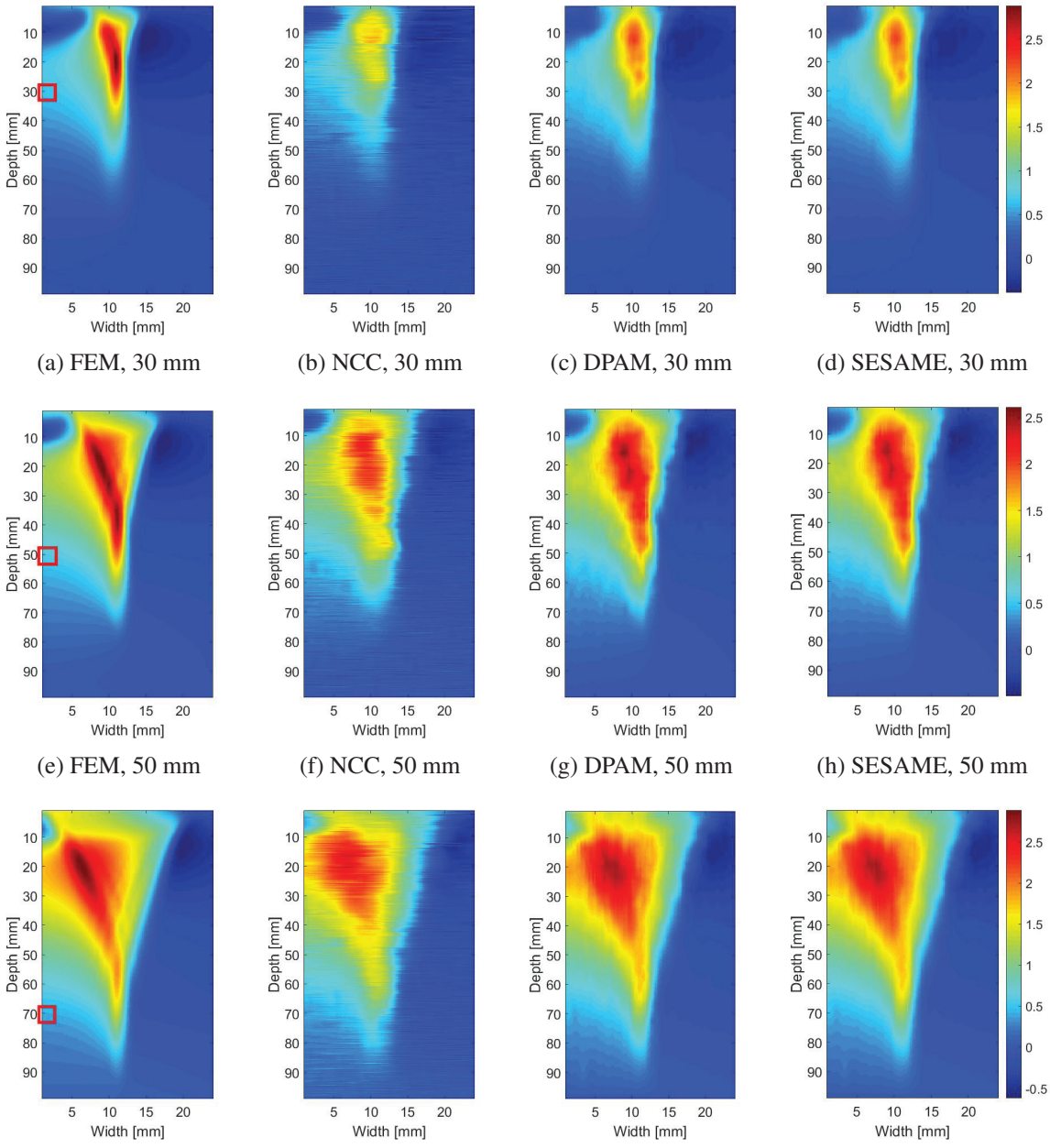

(a) FEM, 30 mm (b) NCC, 30 mm (c) DPAM, 30 mm (d) SESAME, 30 mm

(e) FEM, 50 mm (f) NCC, 50 mm (g) DPAM, 50 mm (h) SESAME, 50 mm

(i) FEM, 70 mm (j) NCC, 70 mm (k) DPAM, 70 mm (l) SESAME, 70 mm

Figure 5.1: Simulation results for a uniform medium with a shear modulus of 10KPa and F/3.5 focal configuration of 4ms following the excitation. Plot (a) shows the FEM (ground-truth) axial displacement field while plots (b)-(d) are the corresponding displacement fields obtained from NCC, DPAM and SESAME, respectively. Plots (e)-(h) and (i)-(l) are the same as plots (a)-(d) but for excitation focal point of 50 mm and 70 mm, respectively. The focal excitation points are specified by a red squares in plots (a), (e), and (i) at depths of 30mm, 50mm, and 70mm, respectively. The common color-bar (shown on the extreme right hand side) for all plots is shown in μm and illustrates the dynamic range used to display the plots in each row.

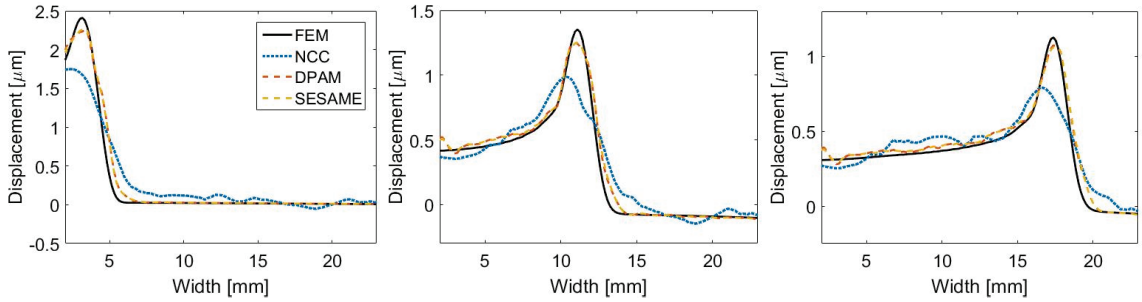

(a) Focal Disp. (t = 1.5 ms) (b) Focal Disp. (t = 4 ms) (c) Focal Disp. (t = 6 ms)

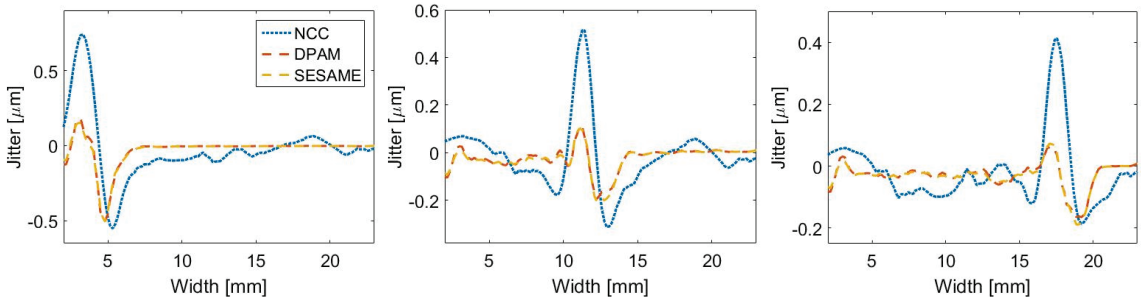

(d) Jitter (t = 1.5 ms) (e) Jitter (t = 4 ms) (f) Jitter (t = 6 ms)

Figure 5.2: Displacement field (first row) and jitter (second row) measured at a horizontal line located at the ARF depth at three different time instances following ARF.

estimators show the SNR improvement is achieved over the entire period of time. The error bars are large at the beginning ($t < 1$ ms) and at the end ($t > 3$ ms) of the plot in all cases. The reason is that tracking is difficult immediately following ARF due to initialization, and also a long time following the application of ARF due to attenuation of the shear-waves. This is the same reason why in Fig. 5.2, range of 2-23 mm is used for displacement and jitter reports.

Fig. 5.4 depicts time-step displacements for four independent materials with four different shear moduli of 1, 2, 5, 10KPa at a focal depth of 70mm and a lateral offset of 2.5mm from the excitation point. Higher shear modulus means that tissue is stiffer, which translates to a higher SWS. Comparison of the displacement profiles from (a) to (d) shows that, as expected, the shear-wave propagates faster as μ is increased. NCC suffers from a relatively large underestimation because it assumes constant displacement within the NCC window. In contrast, DPAM and SESAME estimate the displacement field for all samples of the RF data, and as such, the underestimation in displacement is substantially smaller. As shown in all the plots, DPAM and SESAME compared to NCC have smaller deviation in all mediums following the time. Another important point to be noted is higher deviation where the peak displacement happens. That means, tracking displacement of wavefront

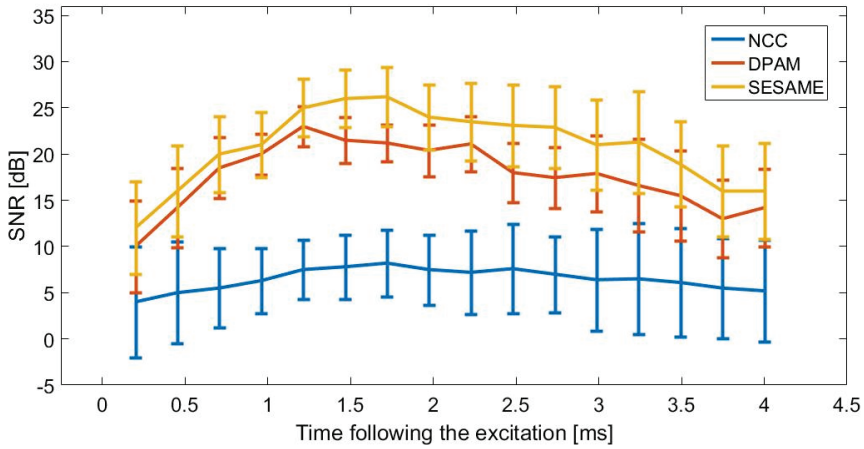

Figure 5.3: Displacement SNR as a function of time following the excitation at the focal depth of 70mm for in a uniform simulation phantom with shear modulus of 10KPa. Error bars show mean and variance over 25 independent realizations.

in almost every medium with different shear modulus values is more difficult that other part of the image.

In Fig. 5.5, the reconstructed shear moduli of the simulation phantom with 10KPa shear modulus is presented. The results are presented for point shear-wave excitation at three focal depths of 30, 50, and 70mm. As explained in subsection 3.4.2, a very outstanding method in order to find elasticity from displacement field is called Time of Flight (TOF) which is referred to time of peak displacement in each specific distance from the excitation point. Herein, displacement fields using all three methods are calculated. Now we determine specific locations in lateral direction along the wave propagation direction. Then we go through all the frames and search for the time (frame-rate is known) where the peak displacement takes place in the selected locations. Now having both distance which the wave is propagated and propagation time, yields SWS and subsequently the shear modulus (Eq. (2)). The results clearly demonstrate that both DPAM and SESAME substantially outperform NCC in both recovering the correct value of the shear modulus and producing a small estimation variance. Similar to the previous simulations, 25 independent realization of the same data is used in calculations which enables us to report deviation as a very significant factor in our assessments. The difference between reconstructed μ averaged over three different depths and true shear modulus are respectively 3.41%, 1.12%, and 1.01% of true μ for NCC, DPAM and SESAME.

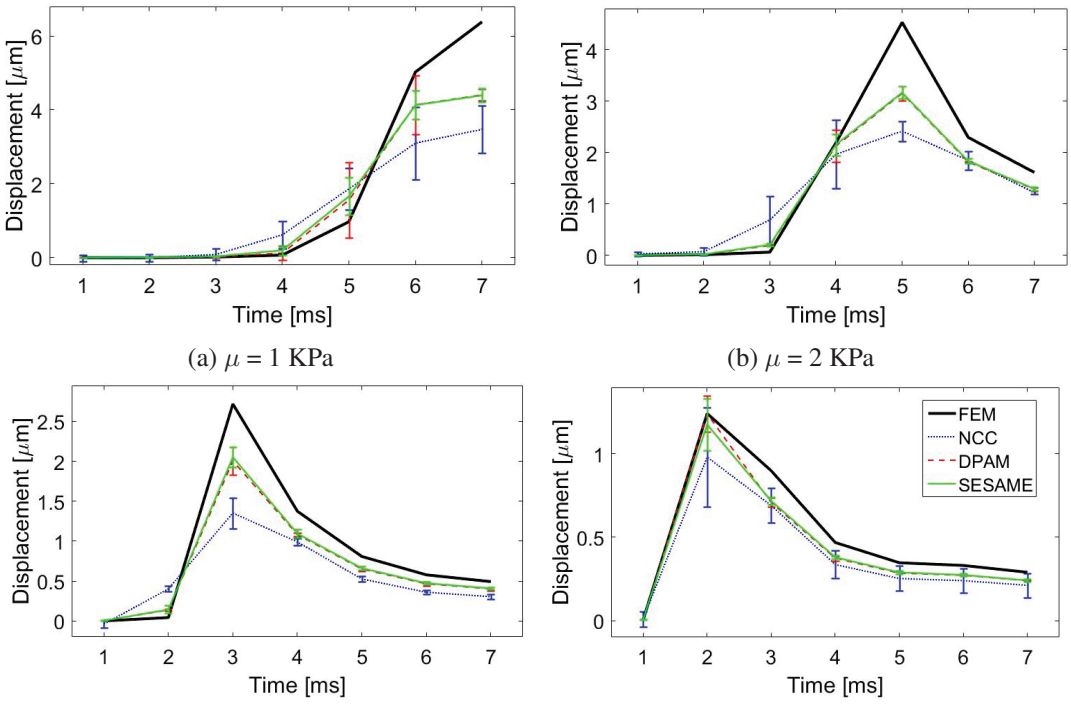

(a) μ = 1 KPa

(b) μ = 2 KPa

(c) μ = 5 KPa

(d) μ = 10 KPa

Figure 5.4: Displacement profile in the simulation experiment at z = ARF depth and 2.5 mm lateral ofset from the ARF focus. Results for four simulation phantoms with different shear modulus (μ) of 1, 2, 5 and 10 KPa are shown. Error bars represent standard deviation of calculated displacements over 25 independent speckle realization. Greater μ relates to stiffer medium which yields faster wave propagation.

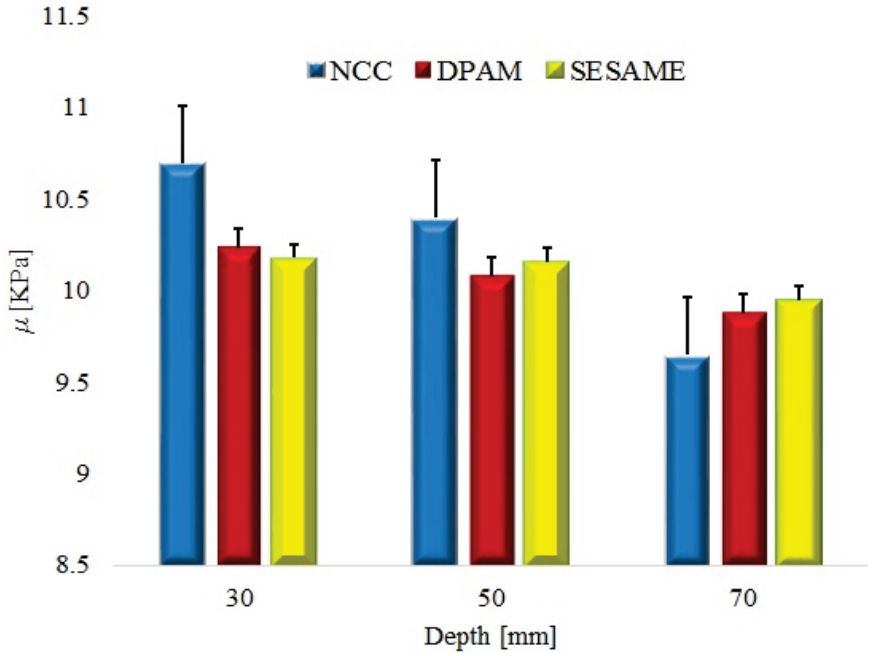

Figure 5.5: Reconstructed shear moduli using displacement estimated using NCC (blue), DPAM (red) and SESAME (yellow) estimators for a uniform simulation phantom for excitation at three different focal points of 30, 50 and 70 mm. True shear modulus is 10 KPa. Bars and error bars respectively represent mean and variance over 25 independent realization.

5.2 Phantom Studies

In this section, accuracy and precision of the proposed methods is assessed using real experimental data. First we present results of uniform phantom and then shown the results in presence of lesion. In imaging every part of the phantom (background, lesion 1, and lesion 2), some points should be noted that are summuarized in the following:

(1) Background: This region which is a uniform region represents healthy part of the tissue. Uniform part has μ of 2.33KPa. We choose an area where lesion are not located there and start imaging there. Excitation happens at depth of 2cm and using all the methods, we first track the deformation and reconstruct SWS and then shear modulus using TOF approach. In this experiment, displacement field, SNR, and reconstructed μ is reported which all the results, illustrate accuracy and precision of the proposed methods.

(2) Lesion 1: The lesion is located in depth of 3cm in the phantom and has μ of 7KPa. We first find it using normal mode of ultrasound machine and then will fix the probe and start imaging

the medium. Excitation occurs very close to the lesion in order to ensure wave propagates in the lesion. Reconstructed μ shows how the proposed methods result in more accurate μ.

(3) Lesion 2: This lesion is also located in depth of 3cm in the phantom and has μ of 15KPa. Again like what we do for lesion 1, we first find it using normal mode of ultrasound machine and then will fix the probe and start imaging the phantom. Similar to experiment on lesion 1, we excite a very close area to the lesion in order to ensure wave propagates in the lesion. Reconstructed μ shows how the proposed methods yielded more precise results of μ.

These experiments will be explained in more details in the following. All the data presented in this section are acquired by the author and supervisors.

5.2.1 Uniform Phantom Experiment

In this experiment, a region in the background which is uniform is selected. In order to make sure we are not imaging lesion parts, first in normal mode of ultrasound scanner, we scan the phantom an find where exactly two lesions are placed. Then, we choose a region far away of the lesion and then we start shear-wave imaging. The procedure of uniform data collection in more details is as following:

(1) Typically a few ultrasound probes are connected to a machine for various purposes. First, we set the L3-8 transducer which we use in this work.

(2) Phantom should be placed in flat place and be fixed during the entire experiment.

(3) Now we scan the phantom in normal mode of the scanner to display the lesions on the screen and find the location of the lesions.

(4) We move away of the lesions to a uniform place and then we hold the probe with any movement.

(5) In Alpinion ultrasound machine, to set the parameters of imaging such as frequency, pulse repetition, focal depth and etc, we are supposed to give desired values to the parameters and

compile the code. Once code is compiled, an executive file is created. Then we run the executive file and imaging starts.

(6) Once the imaging is started, after severals seconds, we can pause the imaging and transfer the data stored in the buffer to the system memory.

(7) Stored data are in format of ".mat" and are transferred to the computer for processing.

After storing the data in the computer, we unpack the data to form RF data which is desired for displacement estimating. Afterward, we calculate displacement frames using NCC, DPAM and SESAME and then will try to reconstruct elasticity using SWS. In simulations, ground-truth displacement is provided. Therefore, for accuracy assessment, we always compare with ground-truth. Here ground-truth displacement is unknown but producer of the phantom has provided to us exact values of elasticity everywhere in the phantom. As a result, we take the elasticity value as our ground-truth and compare the reconstructed value we obtain from acquired data with given elasticity values. In the following, displacement field, SNR and elasticity values are shown.

Fig. 5.6 depicts displacement field estimated using NCC, DPAM and SESAME methods over the B-mode image of the same location. Excitation focal point is 24cm and the displacement frames are corresponded to 2.2msec following the excitation. In shear-wave imaging, displacements are in order of micrometer and that is why color-bars are showed in micrometer. As clearly visible, SESAME and DPAM result in a very smooth displacement image which helps us in detecting and following the wavefront in the displacement frames.

Fig. 5.7 plots the signal-to-noise ratio (SNR) as a function of time following the ARF excitation focused at a depth of 2cm. The experiment is repeated 25 times by randomly relocating the ultrasound probe. Blue, red and yellow curves correspond to the SNR values obtained from NCC, DPAM and SESAME, respectively. The error bars in Fig. 5.7 represent standard deviations over 25 experiments. Both DPAM and SESAME outperform NCC substantially and, on average, yield respective improvements of 7.6dB and 9.5dB in the displacement SNR. In addition, the results illustrate that approximately 7ms following the excitation, NCC SNR drops below 0dB while DPAM and SESAME maintain relatively high SNR values.

Fig. 5.8 shows reconstructed shear modulus μ of the phantom with a ground truth value for μ

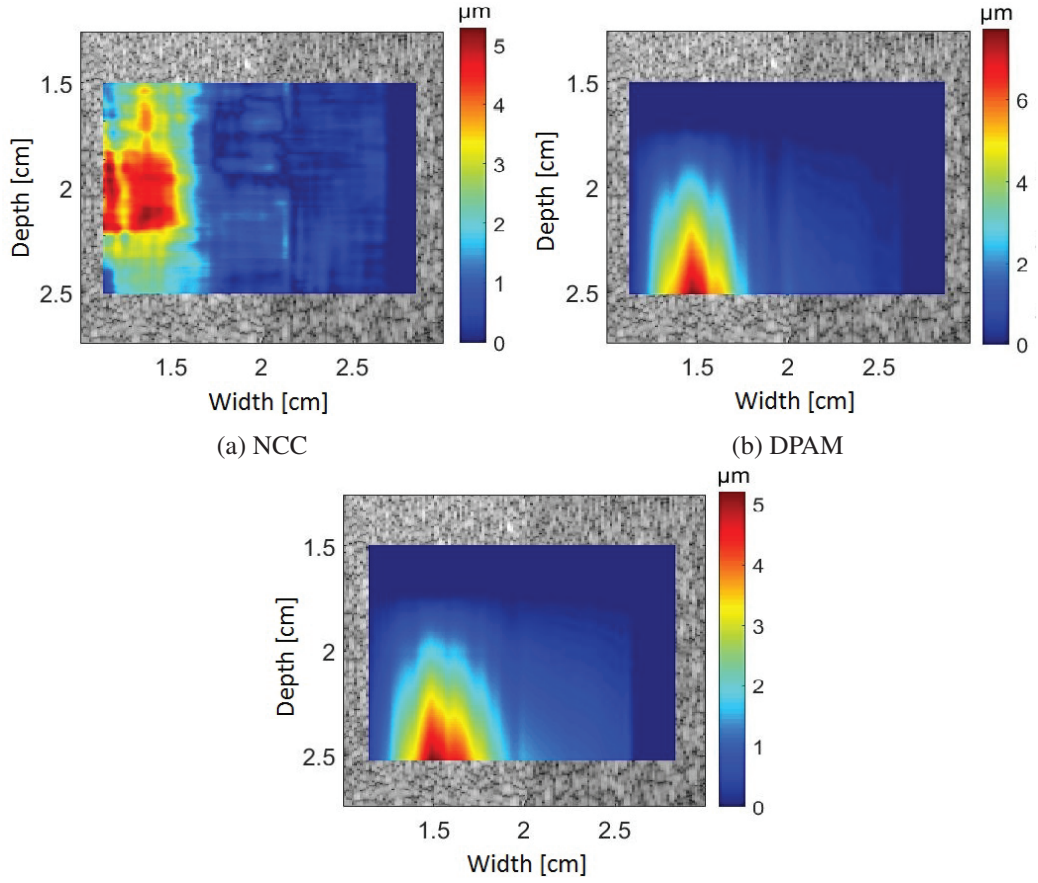

(a) NCC

(b) DPAM

(c) SESAME

Figure 5.6: Displacement field in uniform area of CIRS phantom 2.2msec following the excitation. Excitation focal point is 2cm.

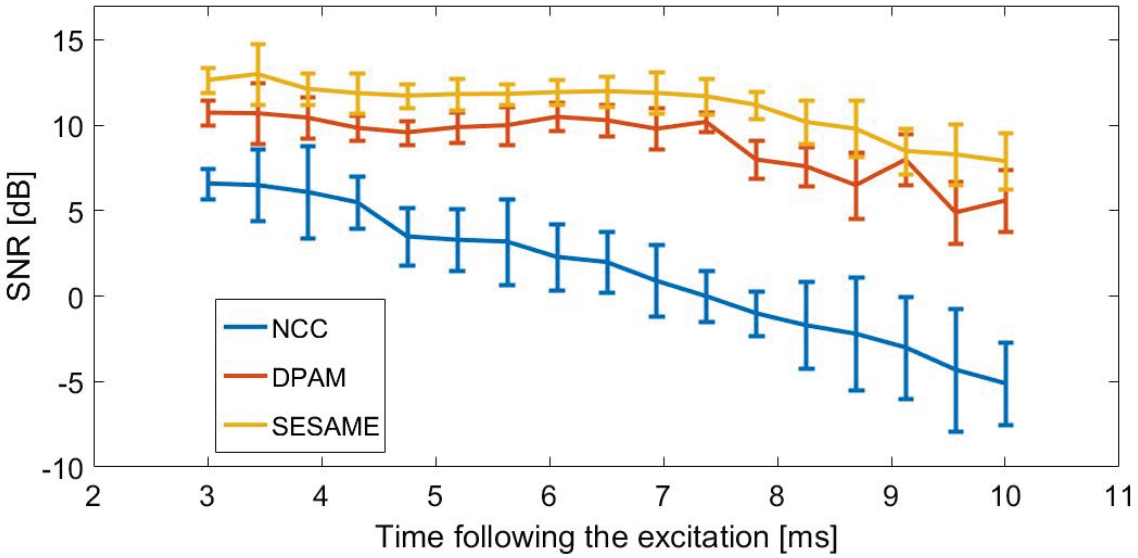

Figure 5.7: Displacement SNR as a function of time following the excitation at the focal depth of 20 mm in the ROI. Error bars show mean and variance over 25 data collections from the same phantom. NCC curve falls under 0 dB approximately after the wave travels for 7 ms due to the attenuation of the displacement amplitude.

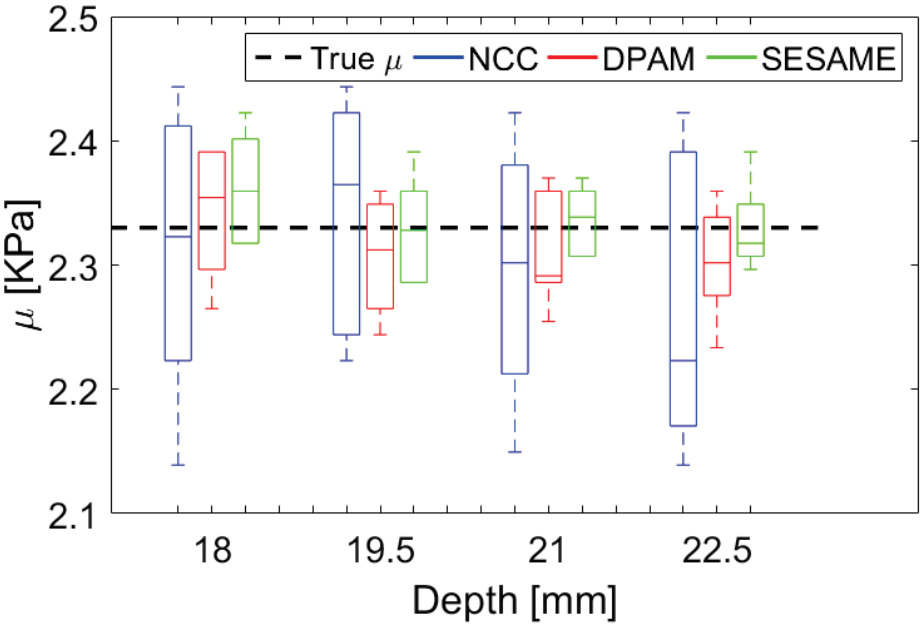

Figure 5.8: Reconstructed shear moduli measured in ROI at four different depths. The excitation is at 20 mm depth. Tracking wavefront is done using NCC (blue), DPAM (red) and SESAME (yellow) in a tissue-mimicking phantom with given shear modulus of 2.33KPa (black horizontal dashed line). Data collection is repeated 25 times at different locations of the phantom. From top to bottom, each bar shows maximum, 75%, median, 25% and maximum values.

of 2.33KPa and material density of 1.03g/cm^3 for the four depths of 18, 19.5, 21, and 22 mm, μ is calculated from SWS. As described in the literature review previously, in soft tissue, elasticity or Young's modulus is almost three times shear modulus. Therefore, 2.33KPa as the shear modulus is the same as 7KPa as elasticity. The ground truth value is shown with a dashed line, and the results obtained from the NCC, DPAM and SESAME results are displayed in blue, red and yellow lines, respectively. The values of the bars from top to bottom respectively correspond to maximum, 75th percentile, median, 25 percentile and minimum measurements. Both DPAM and SESAME estimators yield a better performance in terms of both bias and variance. A comparison between DPAM and SESAME shows further improvements in estimating shear-wave modulus and corresponding SNR in favor of DPAM in our experiments.

5.2.2 Experiment on a Phantom with Lesion

In this experiment, our goal is to estimate shear modulus of the lesions. To this end, in normal mode of the scanner, we scan the phantom to find the locations where lesions are placed. For lesion 1, once we find the location, probe will be held fixed there by hand and in the setting, we set all the parameters as desired. Setup of imaging the lesion in the phantom is depicted in Fig. 5.9. In order to figure out the steps of imaging and storing the data for processing by more details, the following steps should be noted:

(1) The same as first step in uniform region imaging, first, we set the L3-8 transducer which we use in this work as active probe.

(2) Phantom should be placed in flat place and be fixed during the entire experiment.

(3) Now we scan the phantom in normal mode of the scanner to display the lesions on the screen and find the location of the lesions.

(4) To image each lesion, we place the probe right on top of the lesion such that in normal mode of scanner, the lesion is visible on the screen.

(5) In Alpinion ultrasound machine, to set the parameters of imaging such as frequency, pulse repetition, focal depth and etc, we are supposed to give desired values to the parameters and

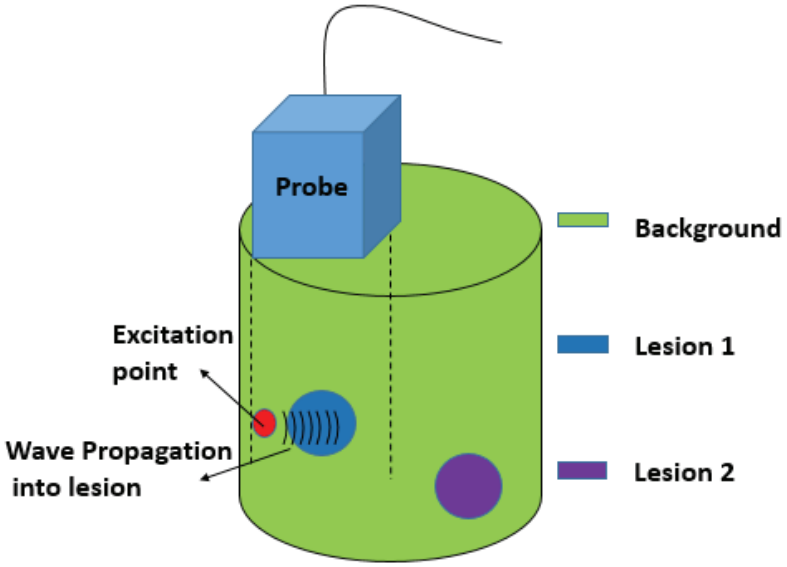

Figure 5.9: Setup regarding imaging the lesion in a CIRS phantom. Probe is located such that covers the lesion. Then by choosing the right location of imaging, a place beside the lesion, as shown by a read circle, is excited and as a result, a transversal wave starts to propagate in the lesion. The idea is to track the wave and then reconstruct elasticity of the lesion using SWS. This plot shows imaging the lesion 1 while imaging lesion 2 will be finding the location of the lesion in phantom and following the same steps.

compile the code. Once code is compiled, an executive file is created. Then we run the executive file and imaging starts.

(6) Once the imaging is started, after several seconds, we can pause the imaging and transfer the data stored in the buffer to the system memory. Because of very high frame-rate of the scanner and limited space of the buffer, only data regarding last 1 sec of the imaging before pausing is available in the buffer.

(7) Stored data are in format of ".mat" and are transferred to the computer for processing.

Every time the phantom excites with a very short pulse, the scanner waits to collects RF information following the excitation for longer time than excitation. In other words, every puch is applied, a set of images is stored which starts with the frame that the medium (phantom or tissue) is at rest and following the frames of deformation happening. Pulse Repetition Frequency (PRF) is a parameter determines how many pushes happen in 1sec and is usually in order of KHz. The data are packed. So for processing, after storing the data in the computer, we unpack the data to

form RF data which is desired for displacement estimating. Afterward, we calculate displacement frames using NCC, DPAM and SESAME and then will try to reconstruct elasticity using SWS along the shear-wave propagation. As previously described in uniform phantom experiment, ground-truth herein is the shear modulus given the the phantom producer. To compare, we only need to reconstruct the shear modulus using acquired data and compare them with the given shear modulus value. This enables us to report quantitative assessment. In the following, reconstructed shear modulus of the lesions is calculated and compared with the real values.

Since lesions in the phantom are supposed as tumors in the body, assessing accuracy of proposed methods and comparing with NCC is very important. This experiment is done using two lesions with higher elasticity values than background in a CIRS phantom and reconstructed shear modulus is calculated and compared with NCC. Fig. 5.10 depicts reconstructed shear modulus μ inside the lesions. Lesions are located 3cm deep in the phantom. We calculate shear modulus at four depths of 28, 29.5, 31, and 32 mm using SWS at these depths. Plot (a) represents reconstructed μ in lesion 1. Blue, red and green bars respectively represent reconstructed values using NCC, DPAM and SESAME. These methods are used for deformation tracking and TOF method is applied then to measure SWS and then μ. Horizontal black dashed-line shows the real value of the μ which is provided by the producer as ground-truth value. Plot (b) is the same as plot (a) but the experiment is done on lesion 2 which contains a material with shear modulus of 15Kpa. The values of the bars from top to bottom respectively correspond to maximum, 75th percentile, median, 25 percentile and minimum measurements. Both DPAM and SESAME estimators yield a better performance in terms of both bias and variance. Furthermore, a comparison between DPAM and SESAME shows improvements in estimating shear modulus using SESAME over DPAM.

5.3 Summary

In this chapter two type of data were used to assess the accuracy and precision of the proposed methods. In fact, we tested the methods to show the accuracy of theoretical and mathematical concepts explained in the previous chapters. To this end, both simulation and real experimental data was used for assessment. In Simulation data, ground-truth was provided by Quantitative Imaging

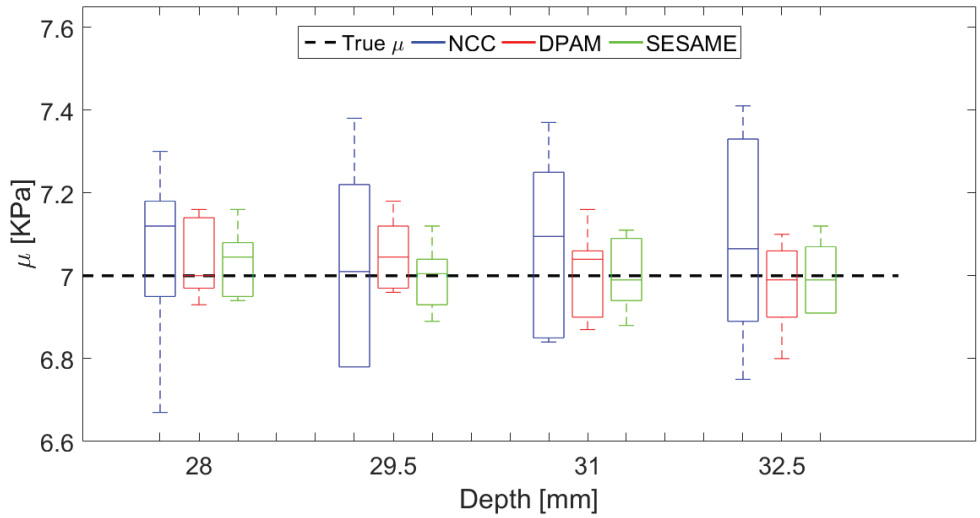

(a) Lesion 1

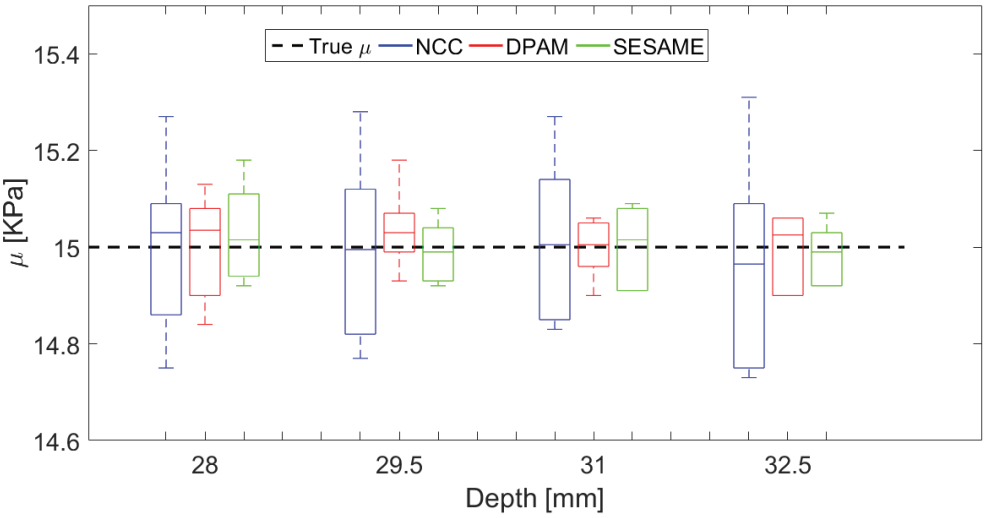

(b) Lesion 2

Figure 5.10: Plots (a) and (b) represent reconstructed shear moduli measured in ROI at four different depths inside the lesion 1 and lesion 2, respectively. The excitation is at 30 mm depth where both lesions are located. Tracking wavefront is done using NCC (blue), DPAM (red) and SESAME (yellow) in a tissue-mimicking phantom with given shear modulus of 7KPa and 15KPa (black horizontal dashed lines) for lesion 1 and lesion 2, respectively. Data collection is repeated 25 times for each lesion. From top to bottom, each bar shows maximum, 75%, median, 25% and minimum values.

Biomarkers Alliance (QIBA). In order to simulate ultrasound RF images, we first simulated a uniform phantom of size $(100 \times 50 \times 20)$ mm in axial, lateral and out-of-plane directions, respectively and then randomly distribute scatterers in the phantom. Number of scatterers determines resolution of ultrasound image. On the other hand, distributing a large number of scatterers, increase the running time of the code to simulate RF image. Herein, we distribute a number of scatterers such that we make sure at least there is 11 scatterers per resolution cell. Next step is using Field II which is an open-source software for simulating ultrasound RF images using the desired parameters for both phantom and probe. every frame is repeated 25 times to also illustrate mean and deviation in our assessment. Simulation is done in three different depths and four different material with different shear modulus. Results of displacement field clearly illustrate superiority of proposed methods in both accurate estimation of displacement and less deviation in measurements. Not only visually assessment proves this idea, but also quantitative measurements such as displacement of a line, jitter, SNR, and shear modulus illustrate superiority of the proposed methods over correlation-based method.

In addition, real data is specifically acquired for this work in PERFORM Centre, Concordia university, Montreal, Canada. In the experiment, a CIRS phantom is used as the medium under imaging and an Alpinion ultrasound machine and L3-8 transducer are used for imaging. Since tumors in the soft organs of body typically consist of stiffer materials, two harder lesion are placed in the phantom by phantom producer and we are given the shear modulus of background and lesions for comparing the obtained results with real values. This experiment is done on all the three regions (background, lesion 1, and lesion 2) of the phantom and results including displacement, SNR and reconstructed shear modulus state the superiority of the proposed methods over NCC.

Chapter 6

Discussion

On one hand, I incorporate prior information of displacement continuity into the cost function to prevent estimating physically unrealistic displacement fields and augment the RF data. On the other hand, I perform global minimization of the cost function to ensure that the optimization procedure is not trapped at a local minima. Our displacement estimation is, therefore, accurate and robust. In contrast to the window-based tracking methods Rouze et al. (2010); Wang et al. (2010), no post-processing step is needed in the proposed approaches.

The proposed DPAM and SESAME outperform NCC in two different aspects. First, the under-estimation of the peak displacement field is much smaller because the displacements are estimated for each sample. In contrast, the window-based methods in essence calculate the average displacement within a window. Therefore, the estimate of peak displacement is severely biased by neighboring samples that have lower displacements. As discussed in detail in Palmeri et al. (2006), this issue is more important in SWE than in quasi-static elastography, since the displacement field is much more uniform in the latter. As verified experimentally, DPAM generates accurate displacement fields for quasi-static elastography and is more suitable for SWE. Second, less noisy displacement fields are generated with DPAM and SESAME without the need for post-processing to eliminate outliers or measurements with higher levels of noise.

I derive a nonlinear cost function with close to a million variables, which is intractable in its original form. We, therefore, linearize the derivative of the cost function to allow for efficient optimization. DPAM ignores second-order derivatives of nonlinear terms, whereas SESAME takes

into account the curvature of the nonlinear terms when linearizing the cost function. An important feature of SESAME is that the derivative of the cost function remains a linear and sparse system despite considering higher order derivatives. Therefore, SESAME outperforms DPAM with only a slightly higher computational complexity.

Both proposed methods are fast enough and suitable for real-time implementation. For instance, to find displacement field between two RF frames of size (1388×150), the DPAM and SESAME estimators on average take 35 and 42ms, respectively, on a single core of a desktop CPU.

Figs. 5.1, 5.2, and 5.3 demonstrate accurate displacement estimation using DPAM and SESAME in a variety of simulations with acoustic radiation force focusing on different excitation regions. In comparison with NCC, the proposed estimators track displacements more accurately such that smaller jitter and higher SNR are obtained. Fig. 5.4 illustrates that NCC, DPAM and SESAME predict faster SWS in a medium with higher elasticity.

The results of Fig. 5.5 demonstrate less variability and more accurate shear modulus (μ) estimation using the proposed methods as compared to NCC. The dependency of shear modulus estimation on excitation focal depth is also described in Wang et al. (2017). Overall, the estimated values of μ averaged over three examined depths are 10.34, 10.11, and 10.10KPa using NCC, DPAM and SESAME for a phantom with a ground truth value of $\mu = 10$KPa.

Chapter 7

Conclusion and Future Work

In the final chapter of this thesis, I summarize the contributions of the thesis and provide some directions for future work. Section 7.1 summarizes the main results of the thesis. Section 7.2 lists the main contributions of this thesis and finally, in Section 7.3, I mention some highlights and possible directions as probable future work that can be followed after this thesis.

7.1 Summary

This thesis explores displacement estimation in shear-wave elastography and addresses some challenging problems related to this application. Challenges in shear-wave elsatography mostly emanate from inaccurate displacement estimation. In addition, real data acquired from ultrasound machine is usually of dimensions 1000×128 which makes real-time implementation of displacement estimators very challenging. Correlation-based methods are commonly used. In these methods, by moving a window in the corresponding image, displacement is estimated by maximizing correlation metrics. Due to insufficient information, these methods usually generate inaccurate displacement fields. By incorporating knowledge of adjacent displacement estimates, many methods have been developed which still suffer from high computation complexity making them infeasible for real-time implementation. The main question this thesis seeks is whether a displacement estimator can be implemented such that it satisfies both accurate displacement estimation and real-time implementation.

In order to answer this question, I proposed two novel methods based on minimizing regularization-based cost function. In these methods, first, an initial guess of displacement on a single RF line is estimated using DP. Two approaches DPAM and SESAME calculate subsample displacement. In shear-wave elastography, in order to come up with an accurate map of elasticity, correct estimation of displacement is highly desired. Using information of adjacent displacement estimates, DPAM and SESAME estimate the deformation with high precision. Both DPAM and SESAME are implemented as MATLAB mex function in C++. Assessing the complexity of these methods mathematically in addition to measuring the execution time confirms the feasibility of these methods for real-time implementation. Reported time are measured using both simulation data and real data. Since SESAME incorporates higher order of Taylor series to estimate non-linear component of the developed cost function, more information is added to the system compared to DPAM. As a result, using SESAME, more accurate displacement is estimated, although the complexity of computation remains almost the same for the two approaches. Results of both simulation data and real data verify the superiority of both SESAME and DPAM over the commonly used NCC approach.

7.2 Contributions

The main contribution of this work is proposing two novel methods for displacement estimation in shear-wave elastography. Current methods in many ultrasound scanners utilize correlation-based estimation, which results in inaccurate displacement map and therefore incorrect estimation of elasticity of the medium under imaging. The proposed methods not only are able to estimate subsample displacement very accurately, they also are highly suitable for real-time implementation. In fact, in elastography, the most challenging part is estimating accurate displacement from raw data acquired from an ultrasound scanner.

As the first contribution, this thesis introduces DPAM for the first time in shear-wave elastography. DPAM has been already successfully applied in the quasi-static elastography Rivaz et al. (2011). This method has shown its superiority in the field of quasi-static elastography over many common methods. DPAM uses DP to first estimate an initial guess of displacement and then further refines that by minimizing a regularized cost function to come up with sub-pixel displacement.

A secondary contribution is using higher second order of Taylor series to estimate nonlinear part in the developed cost function of DPAM. This novel method is called SESAME. Higher order estimation means more information involved and then a more accurate result obtained. As observed in section 4.5, in terms of complexity, SESAME has the same order of complexity as DPAM and both are completely qualified for real-time implementation.

Both DPAM and SESAME can be applied to other elastography techniques such as ARFI imaging. These estimators are implemented in C++ and are able to estimate displacement between two RF image of size 1000×128 in approximately 40msec on a normal desktop computer. As a result, this point plus high accuracy makes them highly appropriate for implementing on real-time ultrasound scanners.

Work explained in this thesis including displacement estimation and shear-wave speed calculation using displacement using real ultrasound data is already peer reviewed in a conference paper Horeh et al. (2017) and a journal version is currently under review by the IEEE Ultrasonics, Ferroelectrics and Frequency Control (UFFC) society.

7.3 Future Work

In this work, only simulation data and real data acquired using CIRS phantom are used for validating the results. Although the proposed methods outperform correlation-based method (NCC) in the performance comparisons based on simulations and real phantom data, verification with real patient data should be considered as future work.

Implementing the proposed algorithms on real scanners and testing performance of these methods can also be considered as future work. Since both methods as observed in the thesis are relatively fast and capable of real-time implementation, this option can provide more accurate estimation compared to available estimators that the scanners commonly use.

In both DPAM and SESAME, a nonlinear term is involved in the cost function. DPAM and SESAME estimators, respectively, use first and second order Taylor series to approximate the nonlinear term. Using nonlinear approximation approaches can be counted as a highly accurate estimation which makes the cost function more precise although it might result in higher complexity.

DP results in an initial guess of displacement on a single RF line and afterward, DPAM and SESAME both estimate subsample displacement of the same RF line. Then the new value is considered as the initial guess for neighboring lines and again the proposed approaches are applied to find displacements of the neighboring RF lines. This procedure continues until the entire displacement image is estimated. Estimating line by line means that inaccurate estimation of one line affects the entire displacement image. As shown in the field of quasi-static elastography Hashemi and Rivaz (2017), this work has the potential to be generalized such that displacement of the entire images is estimated simultaneously.

Appendix A

Field II System

To assess the accuracy of the proposed methods, in addition to real data, we simulated ultrasound data to estimate displacement and shear modulus. In this work, true deformation field was given. In order to simulate ultrasound images, we utilize Field II software Jensen (1996); Jensen and Svendsen (1992). This software is an open-source software. In the following, a brief explaination of the background of this software and simulation using Field II is presented. Fig. A.1 is the logo of Field II software.

A.1 Background

The Field program was first developed by Tupholme and Stepanishen Stepanishen (1971a,7); Tupholme (1969). Using the concept of spatial impulse responses and linear systems theory, Field program tries to find ultrasound image. In fact, the ultrasound probe is excited using a Dirac delta function and as a result, an emitted ultrasound field in a very determined location is created as a function of time. Given excitaion function, by convoving the impulse response with the function, the field will be ontained using any kind of function. The impulse response pf the aperture which is transmitted, is convolved with the excitaion function of the probe. This action results in received response in pulse-echo. Next step is to consider the electro-mechanical function of the probe and to find voltage trace Jensen (1991); Stepanishen (1981). Linear systems theory is used and therefore any excitation can be applied. In the case of continous wave, Fourier transform of the impulse

response in a specific frequecy, gives the appropriate result.

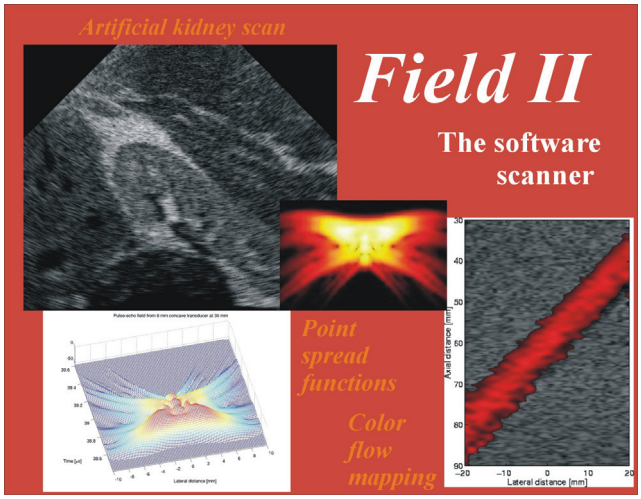

Figure A.1: Field II logo from Field II website $http://field-ii.dk/$.

A.2 Simulation

Depending on geometry of the transducer, different impulse response is obtained. Although for different geometries, this response is calculated, in general speaking, getting a resporesponse for coming up with a single solution for all the geometries is somewhat impossible. In transducers, surface of the transducer is divided into several squares. For each square, impulse response is cacu-lated and sum of the responses yields to the response of the entire transducer Jensen and Svendsen (1992).

Running time of the simulation is always of concern. In order to make the procedure simpler, far-field approximation is used by dividing the transducer into many small squares. Impluse response due to probable discontinuities, are calculated in high frequencies. Therefore, another option in reducing the running time is to use low sampling frequncy. Using integrated impulse response as an additional step, these discontinuities are controlled by Field software which cause no energy to be lost in the impulse response. Although exact response is imoprtant, having no lost is much more significant that getting exact response. For this reason, Field software, usually uses 100MHz as the sampling frequncy. More information can be found in Jensen (1999).

References

Abu-Zidan, F. M., Hefny, A. F., and Corr, P. (2011). Clinical ultrasound physics. *Journal of Emergencies, Trauma and Shock*, 4(4):501.

Aldrich, J. E. (2007). Basic physics of ultrasound imaging. *Critical care medicine*, 35(5):S131–S137.

Bamber, J., Cosgrove, D., Dietrich, C., Fromageau, J., Bojunga, J., Calliada, F., Cantisani, V., Correas, J.-M., Donofrio, M., Drakonaki, E., et al. (2013). Efsumb guidelines and recommendations on the clinical use of ultrasound elastography. part 1: Basic principles and technology. *Ultraschall in der Medizin-European Journal of Ultrasound*, 34(02):169–184.

Bellman, R. E. and Dreyfus, S. E. (2015). *Applied dynamic programming*. Princeton university press.

Bercoff, J., Tanter, M., Chaffai, S., and Fink, M. (2002). Ultrafast imaging of beamformed shear waves induced by the acoustic radiation force. application to transient elastography. In *Proceedings of the 2002 IEEE Ultrasonics Symposium*, volume 2, pages 1899–1902.

Bercoff, J., Tanter, M., and Fink, M. (2004). Supersonic shear imaging: a new technique for soft tissue elasticity mapping. *IEEE transactions on ultrasonics, ferroelectrics, and frequency control*, 51(4):396–409.

Byram, B., Trahey, G. E., and Palmeri, M. (2013). Bayesian speckle tracking. part ii: biased ultrasound displacement estimation. *IEEE transactions on ultrasonics, ferroelectrics, and frequency control*, 60(1):144–157.

Byram, B. C., Trahey, G. E., and Palmeri, M. L. (2012). Effect of prior probability quality on biased

time-delay estimation. *Ultrasonic imaging*, 34(2):65–80.

Carrascal, C. A., Chen, S., Manduca, A., Greenleaf, J. F., and Urban, M. (2017). Improved shear wave group velocity estimation method based on spatiotemporal peak and thresholding motion search. *IEEE Transactions on Ultrasonics, Ferroelectrics, and Frequency Control*.

Catheline, S., Wu, F., and Fink, M. (1999). A solution to diffraction biases in sonoelasticity: the acoustic impulse technique. *The Journal of the Acoustical Society of America*, 105(5):2941–2950.

CRS-SRC (2017). *Incidence of cancer*. https://www.crs-src.ca/page.aspx?pid=1759.

Doherty, J. R., Trahey, G. E., Nightingale, K. R., and Palmeri, M. L. (2013). Acoustic radiation force elasticity imaging in diagnostic ultrasound. *IEEE transactions on ultrasonics, ferroelectrics, and frequency control*, 60(4):685–701.

Dumont, D. M. and Byram, B. C. (2016). Robust tracking of small displacements with a bayesian estimator. *IEEE transactions on ultrasonics, ferroelectrics, and frequency control*, 63(1):20–34.

Dumont, D. M., Walsh, K. M., and Byram, B. C. (2016). Improving displacement signal-to-noise ratio for low-signal radiation force elasticity imaging using bayesian techniques. *Ultrasound in medicine & biology*.

Fahey, B., Nelson, R., Bradway, D., Hsu, S., Dumont, D., and Trahey, G. (2007). In vivo visualization of abdominal malignancies with acoustic radiation force elastography. *Physics in medicine and biology*, 53(1):279.

Fink, M. and Tanter, M. (2011). A multiwave imaging approach for elastography. *Current Medical Imaging Reviews*, 7(4):340–349.

Friedrich-Rust, M., Wunder, K., Kriener, S., Sotoudeh, F., Richter, S., Bojunga, J., Herrmann, E., Poynard, T., Dietrich, C. F., Vermehren, J., et al. (2009). Liver fibrosis in viral hepatitis: noninvasive assessment with acoustic radiation force impulse imaging versus transient elastography 1. *Radiology*, 252(2):595–604.

Gennisson, J.-L., Deffieux, T., Fink, M., and Tanter, M. (2013). Ultrasound elastography: principles and techniques. *Diagnostic and interventional imaging*, 94(5):487–495.

Guo, L., Xu, Y., Xu, Z., and Jiang, J. (2015). A pde-based regularization algorithm toward reducing speckle tracking noise: A feasibility study for ultrasound breast elastography. *Ultrasonic imaging*, 37(4):277–293.

Hashemi, H. S. and Rivaz, H. (2017). Global time-delay estimation in ultrasound elastography. *IEEE Transactions on Ultrasonics, Ferroelectrics, and Frequency Control*.

Hedrick, W. R., Hykes, D. L., and Starchman, D. E. (1995). *Ultrasound physics and instrumentation: practice examinations*. CV Mosby.

Honarvar, M., Rohling, R., and Salcudean, S. (2016). A comparison of direct and iterative finite element inversion techniques in dynamic elastography. *Physics in medicine and biology*, 61(8):3026.

Honarvar, M., Sahebjavaher, R., Rohling, R., and Salcudean, S. (2017). A comparison of fem-based inversion algorithms, local frequency estimation and direct inversion approach used in mr elastography. *IEEE Transactions on Medical Imaging*.

Horeh, M. D., Asif, A., and Rivaz, H. (2017). Regularized tracking of shear-wave in ultrasound elastography. *The 42nd IEEE Int. Conference on Acoustic, Speech and Signal Processing (ICASSP), New Orleans, LA, 2017*, page In press.

Hsu, S. J., Bouchard, R. R., Dumont, D. M., Wolf, P. D., and Trahey, G. E. (2007). In vivo assessment of myocardial stiffness with acoustic radiation force impulse imaging. *Ultrasound in medicine & biology*, 33(11):1706–1719.

Hsu, S. J., Hubert, J. L., Smith, S. W., and Trahey, G. E. (2008). Intracardiac echocardiography and acoustic radiation force impulse imaging of a dynamic ex vivo ovine heart model. *Ultrasonic imaging*, 30(2):63–77.

Jensen, J. A. (1991). A model for the propagation and scattering of ultrasound in tissue. *The Journal of the Acoustical Society of America*, 89:182.

Jensen, J. A. (1996). Field: A program for simulating ultrasound systems. In *10TH Nordic Conference on Biomedical Imaging, VOL. 4, supplement 1, PART 1: 351–353*. Citeseer.

Jensen, J. A. (1999). Linear description of ultrasound imaging systems: Notes for the international summer school on advanced ultrasound imaging at the technical university of denmark.

Jensen, J. A. and Svendsen, N. B. (1992). Calculation of pressure fields from arbitrarily shaped,

apodized, and excited ultrasound transducers. *IEEE transactions on ultrasonics, ferroelectrics, and frequency control*, 39(2):262–267.

Lee, S. Y., Cardones, A. R., Doherty, J., Nightingale, K., and Palmeri, M. (2015). Preliminary results on the feasibility of using arfi/swei to assess cutaneous sclerotic diseases. *Ultrasound in medicine & biology*, 41(11):2806–2819.

McCormick, M., Rubert, N., and Varghese, T. (2011). Bayesian regularization applied to ultrasound strain imaging. *IEEE Transactions on Biomedical Engineering*, 58(6):1612–1620.

McLaughlin, J. and Renzi, D. (2006a). Shear wave speed recovery in transient elastography and supersonic imaging using propagating fronts. *Inverse Problems*, 22(2):681.

McLaughlin, J. and Renzi, D. (2006b). Using level set based inversion of arrival times to recover shear wave speed in transient elastography and supersonic imaging. *Inverse Problems*, 22(2):707.

Nightingale, K. (2011). Acoustic radiation force impulse (arfi) imaging: a review. *Current medical imaging reviews*, 7(4):328–339.

Nightingale, K., McAleavey, S., and Trahey, G. (2003). Shear-wave generation using acoustic radiation force: in vivo and ex vivo results. *Ultrasound in medicine & biology*, 29(12):1715–1723.

Nightingale, K. R., Palmeri, M. L., Nightingale, R. W., and Trahey, G. E. (2001). On the feasibility of remote palpation using acoustic radiation force. *The Journal of the Acoustical Society of America*, 110(1):625–634.

Oliphant, T. E., Manduca, A., Ehman, R. L., and Greenleaf, J. F. (2001). Complex-valued stiffness reconstruction for magnetic resonance elastography by algebraic inversion of the differential equation. *Magnetic resonance in Medicine*, 45(2):299–310.

Ophir, J., Garra, B., Kallel, F., Konofagou, E., Krouskop, T., Righetti, R., and Varghese, T. (2000). Elastographic imaging. *Ultrasound in medicine & biology*, 26:S23–S29.

Palmeri, M. and Qiang, B. (2016). Rsna-qiba-us-sws/qiba-digitalphantoms v1.0.0.

Palmeri, M. L., McAleavey, S. A., Trahey, G. E., and Nightingale, K. R. (2006). Ultrasonic tracking of acoustic radiation force-induced displacements in homogeneous media. *IEEE transactions on ultrasonics, ferroelectrics, and frequency control*, 53(7):1300–1313.

Palmeri, M. L., Qiang, B., Chen, S., and Urban, M. W. (2017). Guidelines for finite-element modeling of acoustic radiation force-induced shear wave propagation in tissue-mimicking media. *IEEE Transactions on Ultrasonics, Ferroelectrics, and Frequency Control*, 64(1):78–92.

Palmeri, M. L., Sharma, A. C., Bouchard, R. R., Nightingale, R. W., and Nightingale, K. R. (2005). A finite-element method model of soft tissue response to impulsive acoustic radiation force. *IEEE transactions on ultrasonics, ferroelectrics, and frequency control*, 52(10):1699–1712.

Palmeri, M. L., Wang, M. H., Dahl, J. J., Frinkley, K. D., and Nightingale, K. R. (2008). Quantifying hepatic shear modulus in vivo using acoustic radiation force. *Ultrasound in medicine & biology*, 34(4):546–558.

Pellot-Barakat, C., Lefort, M., Chami, L., Labit, M., Frouin, F., and Lucidarme, O. (2015). Automatic assessment of shear wave elastography quality and measurement reliability in the liver. *Ultrasound in medicine & biology*, 41(4):936–943.

Redford, D. T. (2006). Understanding ultrasound physics. *Anesthesia & Analgesia*, 102(1):337.

Rivaz, H. (2015). Incorporating second-order derivatives into real-time regularized ultrasound elastography. *Int. Tissue Elasticity Conference ITEC*.

Rivaz, H., Boctor, E., Foroughi, P., Zellars, R., Fichtinger, G., and Hager, G. (2008). Ultrasound elastography: a dynamic programming approach. *Medical Imaging, IEEE Transactions on*, 27(10):1373–1377.

Rivaz, H., Boctor, E. M., Choti, M. A., and Hager, G. D. (2011). Real-time regularized ultrasound elastography. *IEEE transactions on medical imaging*, 30(4):928–945.

Rivaz, H., Boctor, E. M., Choti, M. A., and Hager, G. D. (2014). Ultrasound elastography using multiple images. *Medical image analysis*, 18(2):314–329.

Rivaz, H., Boctor, E. M., and Fichtinger, G. (2006). P3e-9 ultrasound speckle detection using low order moments. In *2006 IEEE Ultrasonics Symposium*, pages 2092–2095. IEEE.

Rouze, N. C., Wang, M. H., Palmeri, M. L., and Nightingale, K. R. (2010). Robust estimation of time-of-flight shear wave speed using a radon sum transformation. *IEEE transactions on ultrasonics, ferroelectrics, and frequency control*, 57(12):2662–2670.

Sandrin, L., Tanter, M., Catheline, S., and Fink, M. (2002). Shear modulus imaging with 2-d transient elastography. *IEEE transactions on ultrasonics, ferroelectrics, and frequency control*,

49(4):426–435.

Sarvazyan, A. P., Rudenko, O. V., Swanson, S. D., Fowlkes, J. B., and Emelianov, S. Y. (1998). Shear wave elasticity imaging: a new ultrasonic technology of medical diagnostics. *Ultrasound in medicine & biology*, 24(9):1419–1435.

Sharma, A. C., Soo, M. S., Trahey, G. E., and Nightingale, K. R. (2004). Acoustic radiation force impulse imaging of in vivo breast masses. In *Ultrasonics Symposium, 2004 IEEE*, volume 1, pages 728–731. IEEE.

Sinkus, R., Tanter, M., Xydeas, T., Catheline, S., Bercoff, J., and Fink, M. (2005). Viscoelastic shear properties of in vivo breast lesions measured by mr elastography. *Magnetic resonance imaging*, 23(2):159–165.

Stepanishen, P. R. (1971a). The time-dependent force and radiation impedance on a piston in a rigid infinite planar baffle. *The Journal of the Acoustical Society of America*, 49(3B):841–849.

Stepanishen, P. R. (1971b). Transient radiation from pistons in an infinite planar baffle. *The Journal of the Acoustical Society of America*, 49(5B):1629–1638.

Stepanishen, P. R. (1981). Pulsed transmit/receive response of ultrasonic piezoelectric transducers. *The Journal of the Acoustical Society of America*, 69(6):1815–1827.

Sumi, C. (2005). Usefulness of ultrasonic strain measurement- based shear modulus reconstruction for diagnosis and thermal treatment. *IEEE Trans. Ultrason. Ferroelectr. Freq. Control*, 52(10):1670 – 1689.

Tanter, M., Bercoff, J., Athanasiou, A., Deffieux, T., Gennisson, J.-L., Montaldo, G., Muller, M., Tardivon, A., and Fink, M. (2008). Quantitative assessment of breast lesion viscoelasticity: initial clinical results using supersonic shear imaging. *Ultrasound in medicine & biology*, 34(9):1373–1386.

Tupholme, G. E. (1969). Generation of acoustic pulses by baffled plane pistons. *Mathematika*, 16(2):209–224.

Van Houten, E. E., Doyley, M. M., Kennedy, F. E., Weaver, J. B., and Paulsen, K. D. (2003). Initial in vivo experience with steady-state subzone-based mr elastography of the human breast. *Journal of magnetic resonance imaging*, 17(1):72–85.

Wagner, R. F., Smith, S. W., Sandrik, J. M., and Lopez, H. (1983). Statistics of speckle in ultrasound

b-scans. *IEEE Transactions on sonics and ultrasonics*, 30(3):156–163.

Walker, W. F. and Trahey, G. E. (1994). A fundamental limit on the performance of correlation based phase correction and flow estimation techniques. *IEEE Transactions on Ultrasonics, Ferroelectrics, and Frequency Control*, 41(5):644–654.

Wang, M. H., Palmeri, M. L., Rotemberg, V. M., Rouze, N. C., and Nightingale, K. R. (2010). Improving the robustness of time-of-flight based shear wave speed reconstruction methods using ransac in human liver in vivo. *Ultrasound in medicine & biology*, 36(5):802–813.

Wang, Y., Peng, B., and Jiang, J. (2017). Building an open-source simulation platform of acoustic radiation force-based breast elastography. *Physics in Medicine and Biology*, 62(5):1949.

Zhai, L., Madden, J., Foo, W.-C., Palmeri, M. L., Mouraviev, V., Polascik, T. J., and Nightingale, K. R. (2010). Acoustic radiation force impulse imaging of human prostates ex vivo. *Ultrasound in medicine & biology*, 36(4):576–588.